

# Quarkonium Production

R. Vogt

Lawrence Livermore National Laboratory, Livermore, CA 94551, USA  
Physics Department, University of California, Davis, CA 95616, USA

- $pp$  Collisions
- $pA$  and  $dA$  Collisions

# Introduction to Quarkonium

$S$  state quarkonium detected through measurements of decays to lepton pairs,  $P$  states detected through radiative decays to an  $S$  state plus a photon

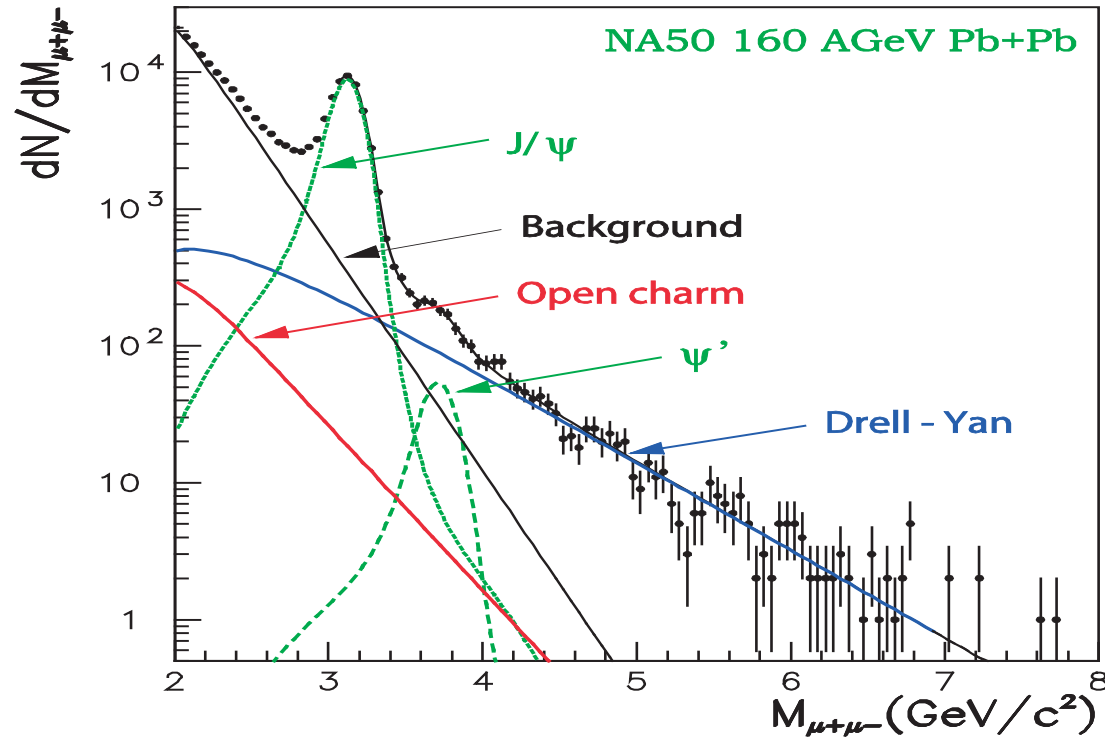


Figure 1: Example of contributions to the dimuon mass distribution at fixed-target energies.  $\Upsilon$  production is negligible at this energy.

# Quarkonium States

State $\mathcal{C}$	$n^{2S+1}L_J$	$J^{PC}$	Mass (GeV)	$B(\mathcal{C} \rightarrow \mu^+\mu^-)$
$J/\psi$ [ $\psi(1S)$ ]	$1^3S_1$	$1^{--}$	<b>3.097</b>	$0.0588 \pm 0.0010$
$\chi_{c0}$	$1^3P_0$	$0^{++}$	<b>3.415</b>	—
$\chi_{c1}$	$1^3P_1$	$1^{++}$	<b>3.511</b>	—
$\chi_{c2}$	$1^3P_2$	$2^{++}$	<b>3.556</b>	—
$\psi'$ [ $\psi(2S)$ ]	$2^3S_1$	$1^{--}$	<b>3.686</b>	$0.0073 \pm 0.0008$
$\Upsilon$ [ $\Upsilon(1S)$ ]	$1^3S_1$	$1^{--}$	<b>9.460</b>	$0.0248 \pm 0.0006$
$\chi_{b0}(1P)$	$1^3P_0$	$0^{++}$	<b>9.860</b>	—
$\chi_{b1}(1P)$	$1^3P_1$	$1^{++}$	<b>9.893</b>	—
$\chi_{b2}(1P)$	$1^3P_2$	$2^{++}$	<b>9.913</b>	—
$\Upsilon'$ [ $\Upsilon(2S)$ ]	$2^3S_1$	$1^{--}$	<b>10.023</b>	$0.0131 \pm 0.0021$
$\chi_{b0}(2P)$	$2^3P_0$	$0^{++}$	<b>10.232</b>	—
$\chi_{b1}(2P)$	$2^3P_1$	$1^{++}$	<b>10.255</b>	—
$\chi_{b2}(2P)$	$2^3P_2$	$2^{++}$	<b>10.269</b>	—
$\Upsilon''$ [ $\Upsilon(3S)$ ]	$3^3S_1$	$1^{--}$	<b>10.355</b>	$0.0181 \pm 0.0017$

Table 1: Quarkonium quantum numbers, spins and masses for  $c\bar{c}$  and  $b\bar{b}$  states. The branching ratios to muon pairs are given for the quarkonium  $S$  states.

Separation of direct (and prompt) quarkonium production generally not straightforward due to feed down from higher states

Charmonium states further complicated by their non-prompt contributions from  $b$  meson decays,  $B \rightarrow J/\psi X$ ,  $\psi' X$ , and, at collider energies,  $W^- \rightarrow b\bar{c}X$  followed by  $b\bar{c} \rightarrow c\bar{c} \rightarrow J/\psi, \psi'$

Bottomonium state separation simplified because there is no significant non-prompt production (need virtual  $W^+ \rightarrow t\bar{b} \rightarrow b\bar{b}$ , small since  $m_{W^+} < m_t + m_b$ )



# Bottomonium Family

Extracting direct  $\Upsilon(1S)$  production more complicated: many  $b\bar{b}$  states below the  $B\bar{B}$  threshold

- All  $\Upsilon''$  production is prompt
- Direct  $\Upsilon'$  production requires subtraction of  $\Upsilon'' \rightarrow \Upsilon'$  and  $\chi_b(2P) \rightarrow \Upsilon'$  from inclusive  $\Upsilon'$
- Direct  $\Upsilon$  production requires subtraction of  $\Upsilon'' \rightarrow \Upsilon$ ,  $\chi_b(2P) \rightarrow \Upsilon$ , inclusive  $\Upsilon' \rightarrow \Upsilon$  and inclusive  $\chi_b(1P) \rightarrow \Upsilon$

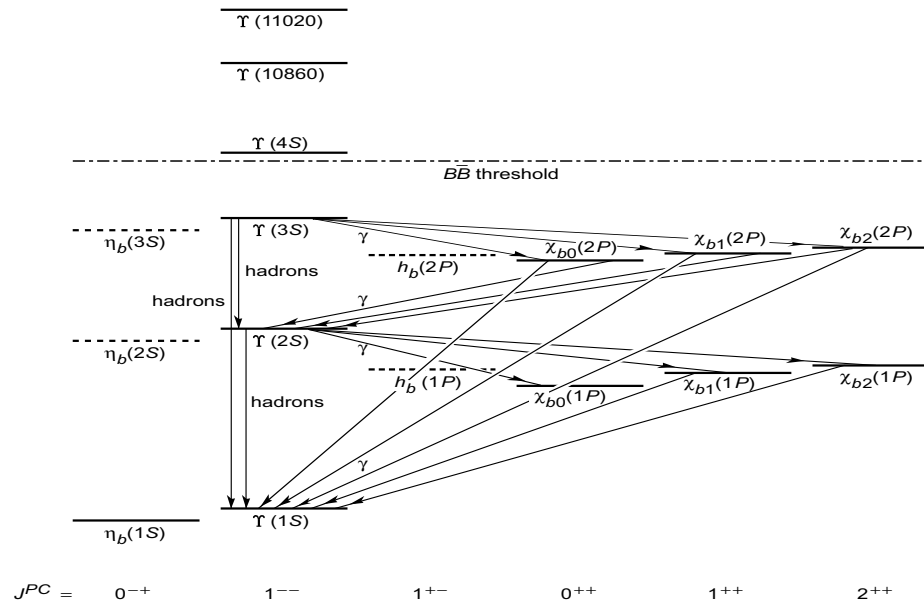


Figure 3: Spectrum of the bottomonium family with important decay transitions between states highlighted.

# Production Models

Scenarios depend on momentum scale  $k$  that turns  $Q\bar{Q}$  pair into quarkonium state

**Color Singlet Model (CSM):**

$k = \mathcal{O}(m_Q)$ , singlet states produced with correct quantum numbers; hard gluon needed for  $S$  state production, e.g.  $gg \rightarrow J/\psi g$ ;  $gg \rightarrow \chi_{c2}$  is direct singlet (Baier *et al.*; Schuler; Lansberg)

**Nonrelativistic QCD (NRQCD) – alias Color Octet Model:**

$k = \mathcal{O}(\alpha_s m_Q)$ , color octet  $Q\bar{Q}$  states converted to final-state color singlets by soft gluon emission; corresponds to velocity  $v = k/m_Q$  expansion; nonperturbative octet and singlet matrix elements fit to data (Braaten, Bodwin and Lepage; Cho and Leibovich; Beneke and Rothstein; Maltoni; Butenschon and Kniehl; many others)

**Intrinsic Charm:**

$k$  soft,  $c\bar{c}$  in proton wavefunction generated by gluons attached to more than one valence quark;  $gc \rightarrow J/\psi c$  provides additional source of high  $p_T$ , forward  $J/\psi$  production (Brodsky and Lansberg)

**Color Evaporation Model (CEM):**

$k = \mathcal{O}(\Lambda_{\text{QCD}})$ ,  $Q\bar{Q}$  quantum numbers changed by soft interactions with probabilities specific to each state but independent of energy (Barger *et al.*; Gavai *et al.*; Schuler and RV; Amundsen *et al.*)

# Calculating Heavy Flavors in Perturbative QCD

‘Hard’ processes have a large scale in the calculation that makes perturbative QCD applicable: high momentum transfer,  $\mu^2$ , high mass,  $m$ , high transverse momentum,  $p_T$ , since  $m \neq 0$ , heavy quark production is a ‘hard’ process

Asymptotic freedom assumed to calculate the interactions between two hadrons on the quark/gluon level but the confinement scale determines the probability of finding the interacting parton in the initial hadron

Factorization assumed between perturbative, calculable hard scattering and the universal, nonperturbative parton distribution functions

Hadronic cross section in an  $AB$  collision where  $AB = pp, pA$  or nucleus-nucleus is

$$\sigma_{AB}(S, m^2) = \sum_{i,j=q,\bar{q},g} \int_{4m_Q^2/s}^1 \frac{d\tau}{\tau} \int dx_1 dx_2 \delta(x_1 x_2 - \tau) f_i^A(x_1, \mu_F^2) f_j^B(x_2, \mu_F^2) \widehat{\sigma}_{ij}(s, m^2, \mu_F^2, \mu_R^2)$$

$f_i^A$  are nonperturbative parton distributions, determined from global fits,  $x_1, x_2$  are momentum fraction of  $A$  and  $B$  carried by partons  $i$  and  $j$ ,  $\tau = s/S$

$\widehat{\sigma}_{ij}(s, m^2, \mu_F^2, \mu_R^2)$  is hard partonic cross section calculable in QCD in powers of  $\alpha_s^{2+n}$ : leading order (LO),  $n = 0$ ; next-to-leading order (NLO),  $n = 1 \dots$

Number of light flavors in  $\alpha_s$  based on mass scale:  $n_{lf} = 3$  for  $c$  and 4 for  $b$

Results depend strongly on quark mass,  $m$ , factorization scale,  $\mu_F$ , in the parton densities and renormalization scale,  $\mu_R$ , in  $\alpha_s$

# Charmonium Production at the Tevatron

Fraction of prompt  $J/\psi$  production from  $\chi_c$  and  $\psi(2S)$  not a strong function of  $p_T$

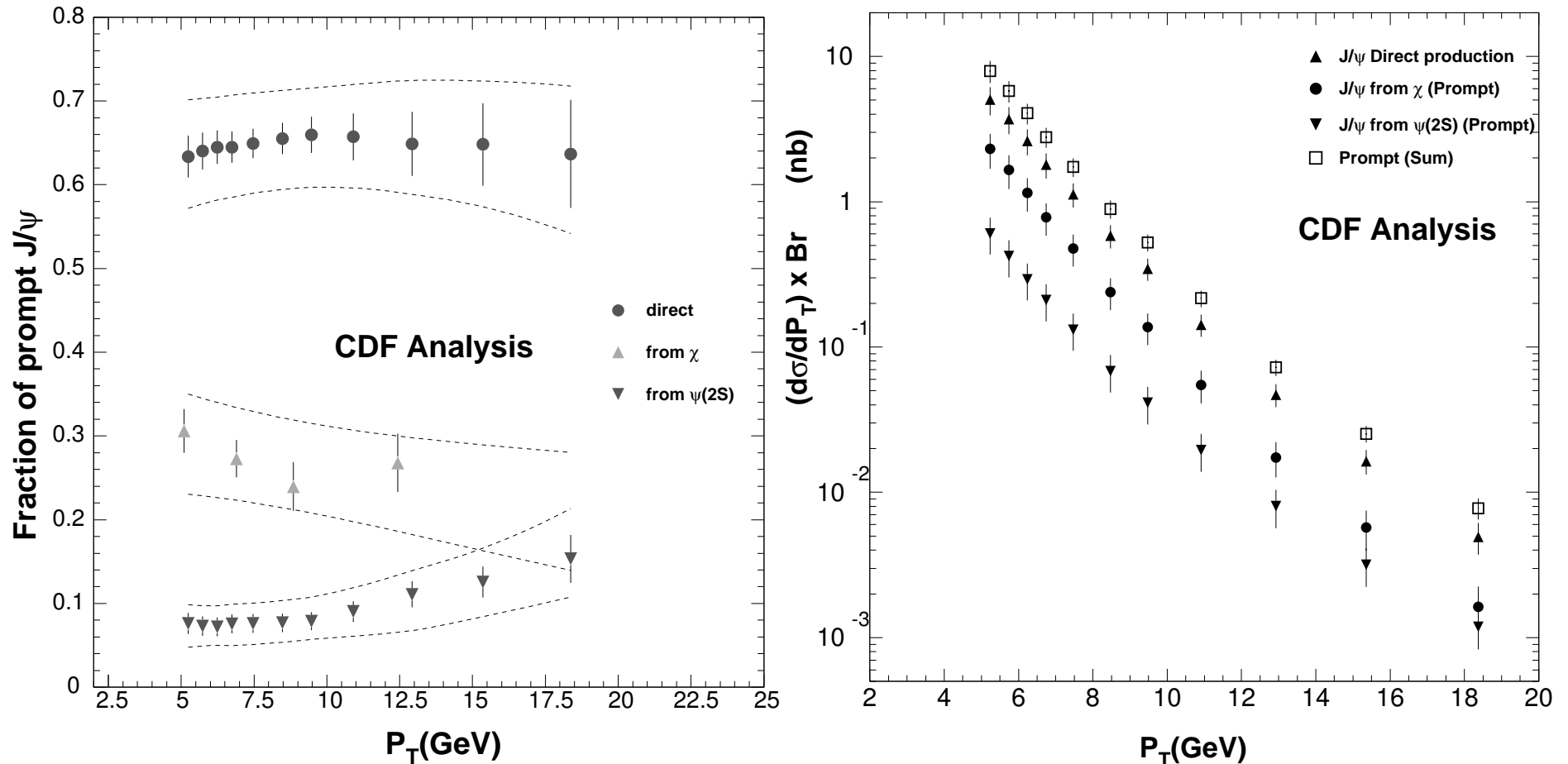


Figure 4: (left) Fraction of prompt  $J/\psi$  production after the  $b$  contribution has been removed. The error bars correspond to statistical uncertainty while the dashed lines are the upper and lower bounds corresponding to the combined statistical and systematic uncertainties. (right) Contributions to the inclusive prompt  $J/\psi$  production in the  $\mu^+\mu^-$  decay channel. From top to bottom the results are total, direct  $J/\psi$ ,  $J/\psi$  from prompt  $\chi_c$  and  $J/\psi$  from prompt  $\psi'$ . [CDF Collab., Phys. Rev. Lett. **79** (1997) 578.]

# Bottomonium Production at $\sqrt{s} = 1.8$ TeV

Independently normalized  $\Upsilon$   $S$  state  $p_T$  distributions agree within statistics

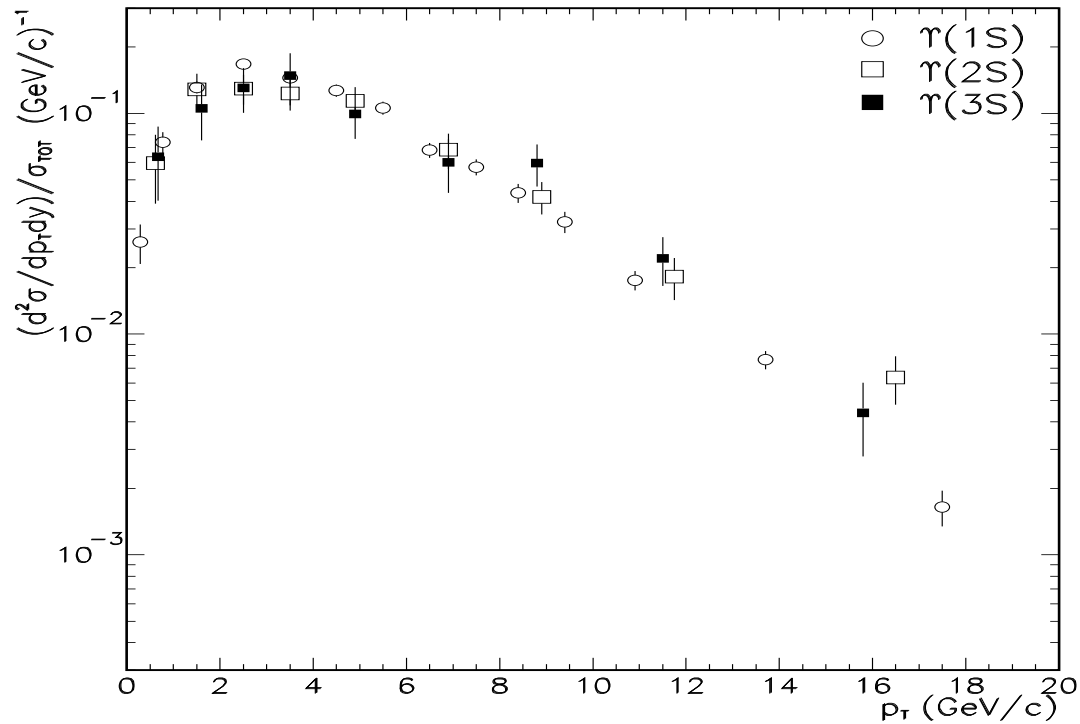


Figure 5: The  $\Upsilon(1S)$ ,  $\Upsilon(2S)$  and  $\Upsilon(3S)$   $p_T$  distributions measured by CDF in the rapidity range  $|y| < 0.4$  normalized to the integrated cross section for each state for better comparison. The error bars are statistical uncertainties only. [CDF Collab., Phys. Rev. Lett. **88** (2002) 161802.]

## $pp$ and $p\bar{p}$ Production

# Color Singlet Model Production

Original CSM assumes factorization of production process into perturbative production of on-shell  $Q$  and  $\bar{Q}$  at scale  $m_T$  of the final state from binding of the pair into a color-singlet meson (assumes that the color and spin of the  $Q\bar{Q}$  pair is unchanged by binding)

Since the  $Q\bar{Q}$  is in a bound state, the heavy quark velocity must be small, thus the bound state is assumed to be created with the heavy quarks at rest in the meson frame, the static approximation

Static approximation amounts to considering only first non-zero part of amplitude when the perturbative matrix element  $\mathcal{M}$  is expanded in powers of relative  $Q\bar{Q}$  momentum  $p$ ; for  $S$  states

$$\int dp \Phi(\vec{p}) \mathcal{M}(p) \delta(2p^0) \simeq \mathcal{M}(p=0) \Psi(\vec{x}=0)$$

Coordinate-space wavefunction  $\Psi$  is non-perturbative input which can be extracted from leptonic decay width:  $|\Psi(0)|^2$  for  $S$  states;  $|\Psi'(0)|^2$  for  $P$  states since  $|\Psi(0)| = 0$

At leading order,  $S$  state production is by  $gg \rightarrow \psi g$  at  $\mathcal{O}(\alpha_s^3)$  while  $gg \rightarrow \chi_c$ ,  $\mathcal{O}(\alpha_s^2)$ , is allowed

Expectation was that prompt  $\psi'$  production should be small and that, at high  $p_T$ , most prompt  $J/\psi$  should come from  $\chi_c$  decays

This expectation remained true even after fragmentation production,  $g \rightarrow \mathcal{C}$  from  $gg \rightarrow gg$  and  $c \rightarrow \mathcal{C}$  from  $Z^0 \rightarrow c\bar{c}$ , dominant at high meson  $p_T$  were considered

# Contributions to CSM $S$ State Quarkonium Production

On-shell heavy quark propagators connected to the bound state

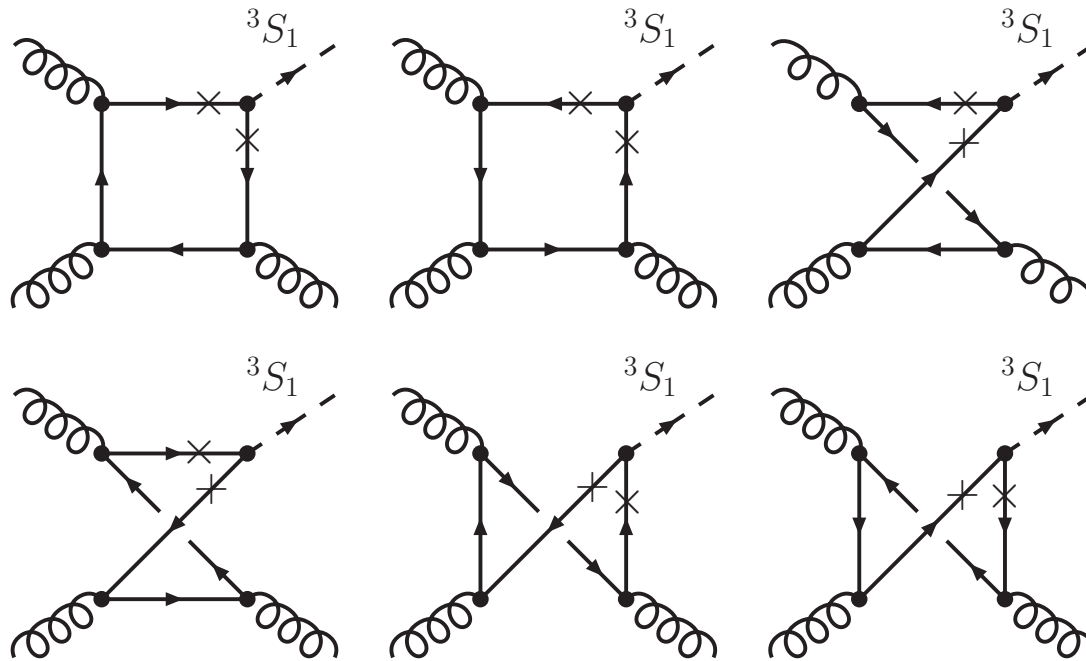


Figure 6: Six diagrams contributing to the leading order CSM cross section of  ${}^3S_1$  states.

# Early Comparison of CSM Predictions to CDF Data

Measured distributions much harder than LO CSM prediction and at least an order of magnitude higher

Including fragmentation contributions increases high  $p_T$  part but does not significantly improve agreement in magnitude (changes slope but not total cross section)

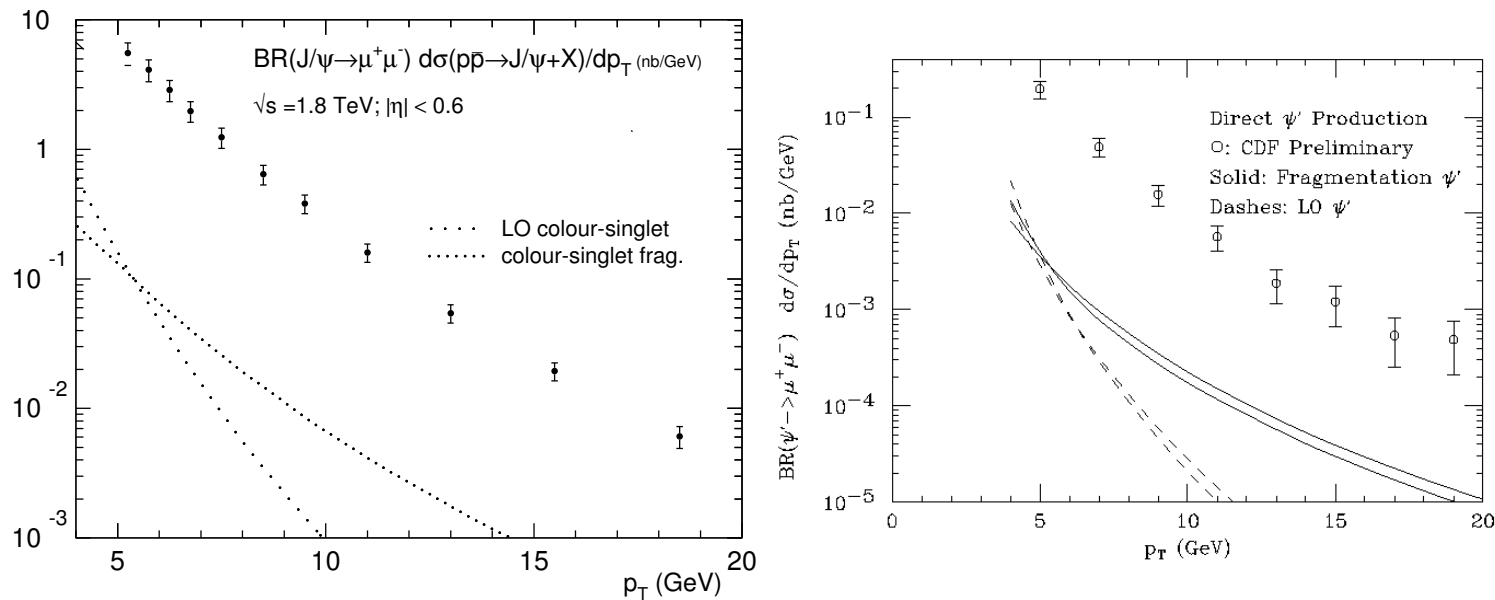


Figure 7: The CSM (including fragmentation)  $p_T$  distributions compared to (left) direct  $J/\psi$  [Prog. Part. Nucl. Phys. **47** (2001) 141] and (right)  $\psi'$  [Phys. Lett. B **333** (1994) 548] measurements by CDF [Phys. Rev. Lett. **79** (1997) 578].

# More Recent CDF Comparisons More Favorable

Higher order contributions to the CSM: complete NLO and a partial NNLO (NNLO<sup>\*</sup>) results bring high  $p_T$  ( $p_T > 5$  GeV) quarkonium production into better agreement with Tevatron data at  $\sqrt{s} = 1.96$  TeV

$J/\psi$  and  $\psi'$  still below the data, cleaner  $\psi'$  has no feed down contribution (all prompt)

$\Upsilon(1S)$  calculation is prompt data (inclusive, *i.e.* with feed down included) times the direct fraction, essentially assuming that the feed down contribution has the same  $p_T$  distribution – similar to CEM, discussed later

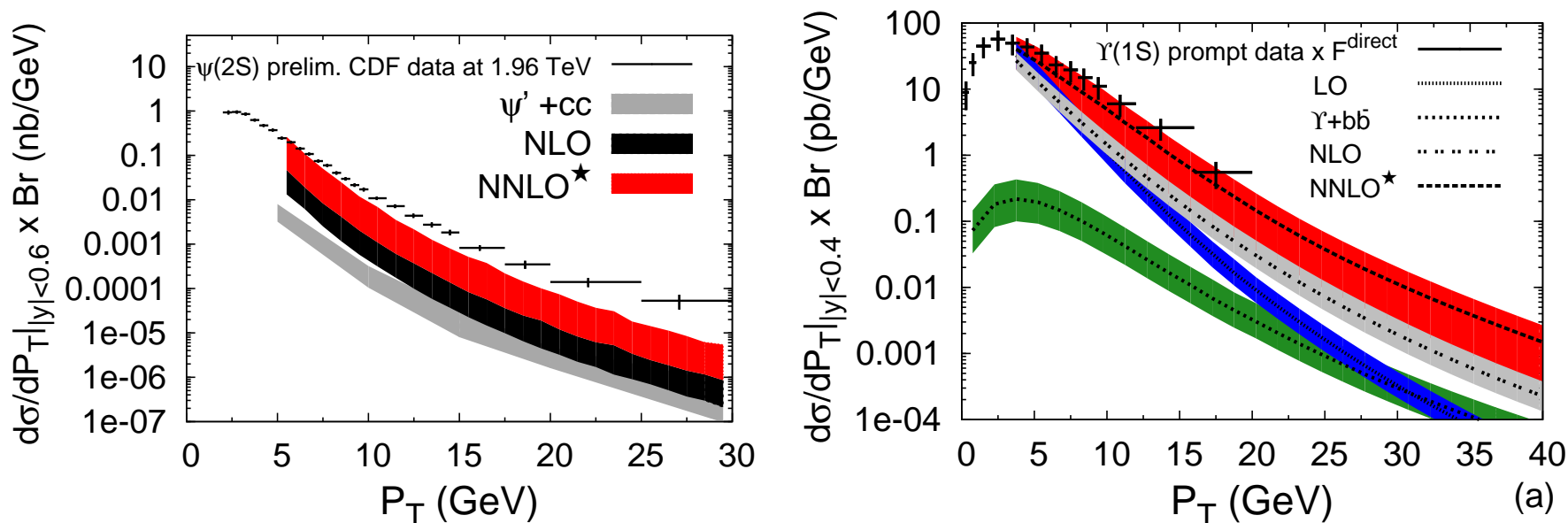


Figure 8: Recent CSM  $p_T$  distributions up to NLO and NNLO<sup>\*</sup> compared to (left)  $\psi'$  and (right)  $\Upsilon(1S)$  measurements by CDF at  $\sqrt{s} = 1.96$  TeV.

# CSM Still Falls Short at RHIC

Calculations for RHIC to NNLO\* at high  $p_T$  including intrinsic charm ( $cg$  LO on plot) agrees with data for  $p_T > 5$  GeV; NLO+ (NLO CSM +  $cg$  LO) falls below medium  $p_T$  data

Rapidity distribution at NLO underestimates PHENIX data, adding intrinsic charm is required to obtain agreement with data

Inclusive  $J/\psi$  data is multiplied by direct fraction of  $J/\psi$  production (data scaled to calculation), assuming feed down contribution has same shape

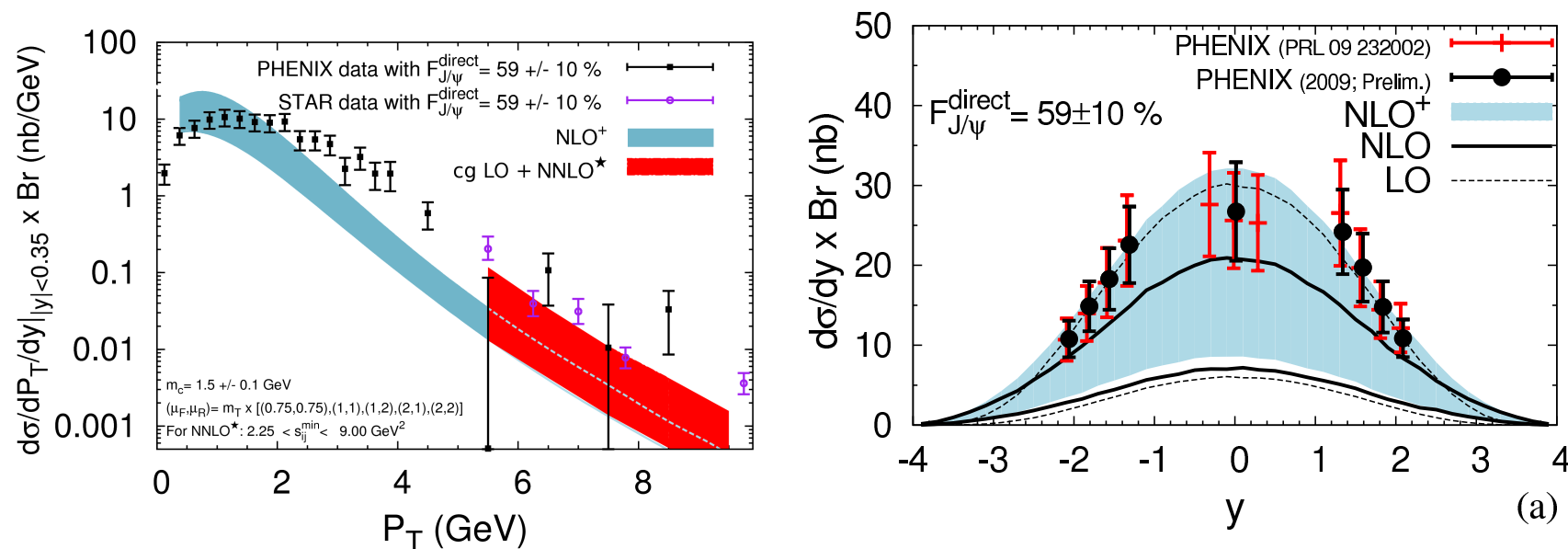


Figure 9: CSM  $p_T$  distributions at NLO+ and NNLO\* +  $cg$  (left)  $\psi'$  and rapidity distributions at LO, NLO and NLO+ (NLO+ = NLO +  $cg \rightarrow J/\psi X$  (right) in  $\sqrt{s} = 200$  GeV  $pp$  collisions at RHIC.

# Color Octet (NRQCD) Production

Starts from Color Singlet Model and adds color octet matrix elements

New Fock states introduced to cancel infrared divergences in light hadron decays of  $\chi_{c1}$  into two gluons, one real and one virtual; when real gluon is soft, decay width diverges without new terms

These new Fock states included  $g\bar{c}c(^3S_1)$  color octet and introduced new momentum scale,  $\Lambda$ , for light quark

Based on systematic expansion in strong coupling constant,  $\alpha_s$ , and relative velocity of  $Q$  and  $\bar{Q}$ ,  $v$  (in bound states,  $v_c^2 \sim 0.23$  and  $v_b^2 \sim 0.08$ )

$$\begin{aligned} |\psi_c\rangle &= \mathcal{O}(1)|Q\bar{Q}[^3S_1^{(1)}]\rangle + \mathcal{O}(v)|Q\bar{Q}[^3P_J^{(8)}]g\rangle + \mathcal{O}(v^2)|Q\bar{Q}[^3S_1^{(1,8)}]gg\rangle + \mathcal{O}(v^2)|Q\bar{Q}[^1S_0^{(8)}]g\rangle + \mathcal{O}(v^2)|Q\bar{Q}[^3D_J^{(1,8)}]gg\rangle + \dots \\ |\chi_{cJ}\rangle &= \mathcal{O}(1)|Q\bar{Q}[^3P_J^{(1)}]\rangle + \mathcal{O}(v)|Q\bar{Q}[^3S_1^{(8)}]g\rangle \end{aligned}$$

Factorization between short distance, perturbative, contribution and non-perturbative hadronization, described by non-perturbative matrix elements in limit of large heavy quark mass

- Two different color singlet matrix elements in NRQCD, one for production and one for decay – can be different even though  $\langle \mathcal{O}^3S_1[^3S_1^{(1)}] \rangle \propto |\Psi(0)|^2$  up to order  $v^4$
- Perturbative octet amplitudes for  $^1S_0^{(8)}$  and  $^3P_0^{(8)}$  have the same  $p_T$  dependence so they can't be separated, thus a linear combination  $\langle \mathcal{O}[^1S_0^{(8)}] \rangle + k \langle \mathcal{O}[^3P_0^{(8)}] \rangle / m_Q^2$  where  $k$  is the ratio of the two amplitudes, typically different for high  $p_T$  (Cho and Leibovich, *etc.*) and fixed-target energies (Beneke and Rothstein)

## A Few Details

More information available on color, spin, and total angular momentum of  $Q\bar{Q}$  pair but more parameters available for fitting to data, increases with order of calculation

Distributions of individual states not necessarily identical

$$\sigma_C^{\text{NRQCD}} = \sum_{i,j} \sum_n \int_0^1 dx_1 dx_2 f_i^A(x_1, \mu^2) f_j^B(x_2, \mu^2) C_{Q\bar{Q}[n]}^{ij}(\mu^2) \langle \mathcal{O}_n^C \rangle$$

$C_{c\bar{c}[n]}^{ij}$ : expansion coefficients in powers of  $\alpha_s(Q^2)$

$\langle \mathcal{O}_n^C \rangle$ : nonperturbative parameters describing the hadronization of state  $C$

Total  $J/\psi$  includes feed down from  $\chi_c$  and  $\psi'$

$$\sigma_{J/\psi} = \sigma_{J/\psi}^{\text{dir}} + \sum_{J=0}^2 B(\chi_{cJ} \rightarrow J/\psi X) \sigma_{\chi_{cJ}} + B(\psi' \rightarrow J/\psi X) \sigma_{\psi'}$$

$\Upsilon$  family more complicated since more states below  $B\bar{B}$  threshold

$$\begin{aligned} \sigma_{\Upsilon} &= \sigma_{\Upsilon}^{\text{dir}} + \sum_{J=0}^2 B(\chi_{bJ}(1P) \rightarrow \Upsilon X) \sigma_{\chi_{bJ}(1P)} + B_{\text{eff}}(\Upsilon(2S) \rightarrow \Upsilon X) \sigma_{\Upsilon(2S)} \\ &+ \sum_{J=0}^2 B_{\text{eff}}(\chi_{bJ}(2P) \rightarrow \Upsilon X) \sigma_{\chi_{bJ}(2P)} + B_{\text{eff}}(\Upsilon(3S) \rightarrow \Upsilon X) \sigma_{\Upsilon(3S)} \end{aligned}$$

$B_{\text{eff}}$  includes direct and chain decays

Octet matrix elements from fits to high  $p_T$  Tevatron data and/or fixed target data

Singlet matrix elements calculated from charmonium wavefunctions at origin

Direct  $J/\psi$  and  $\psi'$  include both singlet (1) and octet (8) contributions to  $gg$  and  $q\bar{q}$

# LO NRQCD Run I Charmonium $p_T$ Distributions

$J/\psi$  and  $\psi'$  color singlet contributions much softer than those of  $\chi_c$

$c\bar{c}[{}^3S_1^{(8)}]$  dominant at high  $p_T$ , hardest  $p_T$  distribution; additional octet contributions give the low  $p_T$  part

Easy enough to fit a  $p_T$  distribution with enough parameters (8 for inclusive  $J/\psi$ )

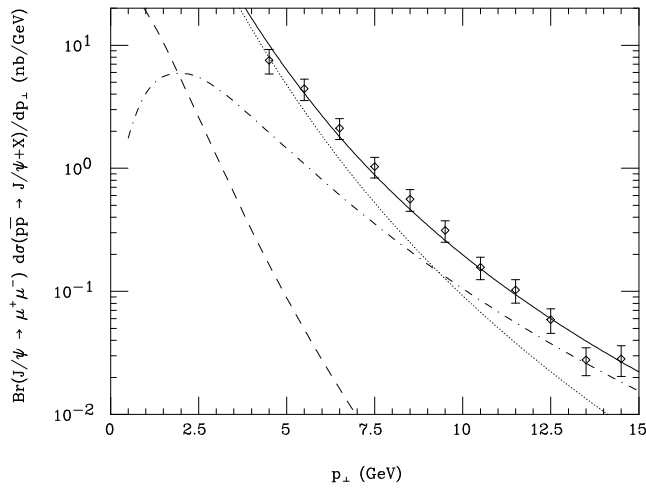


Figure 6

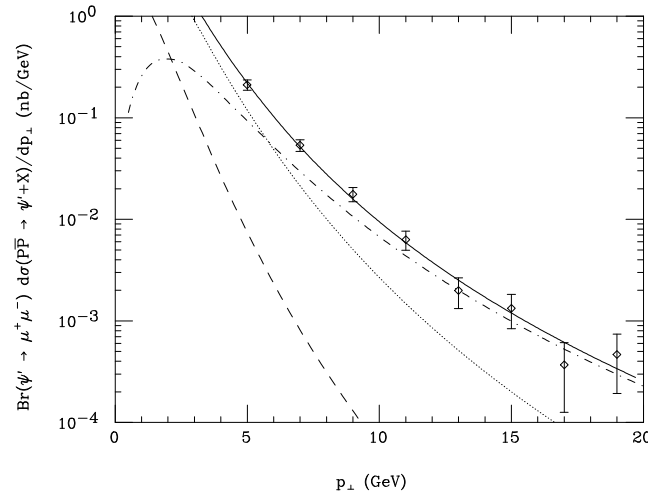


Figure 5

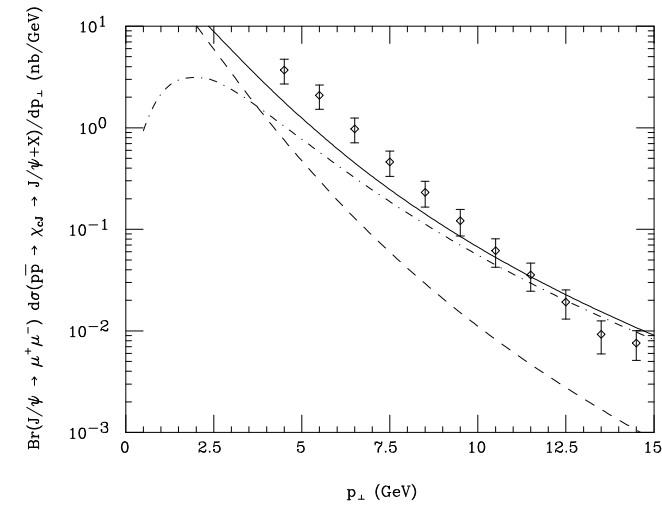


Figure 7

Figure 10: Calculated (left) prompt  $J/\psi$ , (center) prompt  $\psi'$ , and (right)  $J/\psi$ 's from  $\chi_c$  decays compared to CDF Run I data in  $|\eta| \leq 0.6$ . In the left and center plots the dashed curves are the direct color singlet contributions; the dot-dashed curves are the  $c\bar{c}[{}^3S_1^{(8)}]$  contributions; the dotted curves are the combined  $c\bar{c}[{}^P S_J^{(8)}]$  and  $c\bar{c}[{}^1S_0^{(8)}]$  contributions while the solid curve is the sum. The right hand plot shows the color singlet (dashed),  $c\bar{c}[{}^3S_1^{(8)}]$  contribution (dot-dashed) and the sum (solid). All the curves are multiplied by the respective branching ratio to muon pairs. [Phys. Rev. D **53** (1996) 6203.]

# LO NRQCD Run I Bottomonium $p_T$ Distributions

Calculation can only explain high  $p_T$  data

At  $p_T \rightarrow 0$ , need to include intrinsic  $p_T$  broadening or resummation techniques to obtain the correct shape

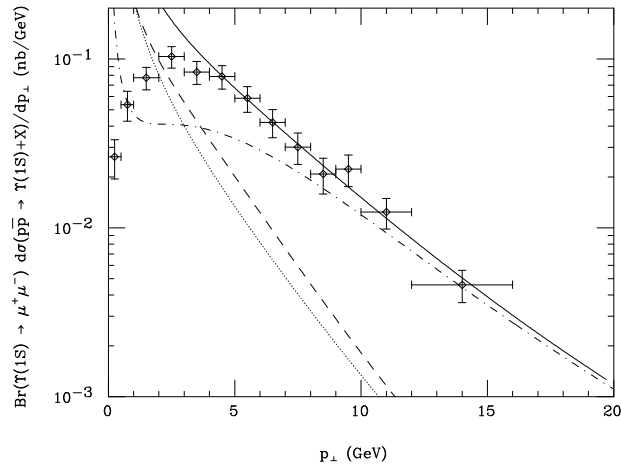


Figure 8

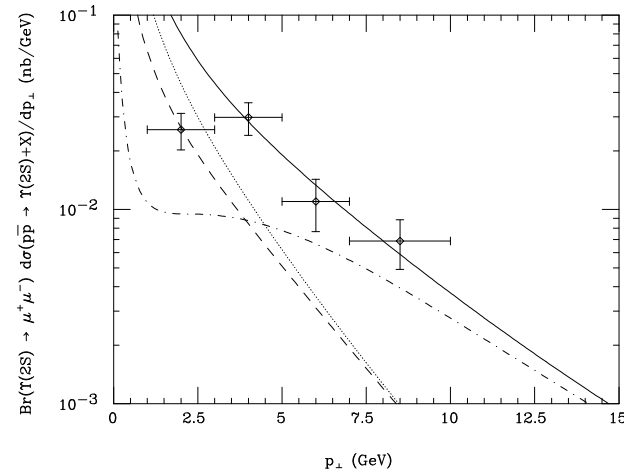


Figure 9

Figure 11: Calculated prompt (left)  $\Upsilon(1S)$  and (right)  $\Upsilon(2S)$  distributions compared to CDF Run I data in the pseudorapidity interval  $|\eta| \leq 0.4$ . In the left and center plots the dashed curves are the direct color singlet contributions; the dot-dashed curves are the  $c\bar{c}[^3S_1^{(8)}]$  contributions; the dotted curves are the combined  $c\bar{c}[^P S_J^{(8)}]$  and  $c\bar{c}[^1S_0^{(8)}]$  contributions while the solid curve is the sum. The right hand plot shows the color singlet (dashed),  $c\bar{c}[^3S_1^{(8)}]$  contribution (dot-dashed) and the sum (solid). All the curves are multiplied by the respective branching ratio to muon pairs. [Phys. Rev. D **53** (1996) 6203.]

# Combined Color Singlet/Color Octet Approach

Global analysis of Butenschon and Kniehl attempts to make global fit to inclusive  $J/\psi$  data from RHIC, Tevatron, LHC (all hadroproduction), and HERA (electroproduction)

Fit LO and NLO color singlet (CS) and NRQCD (CS + CO) calculations to data  
Instead of fitting octet matrix elements to individual data sets, they attempt to obtain universal matrix elements

- Assume a given value of charm quark mass and scales for calculation
- Fit matrix elements with those parameters
- Determine uncertainties on fit results by keeping matrix elements and quark mass fixed, varying scale parameters by a factor of two around central value

Some caveats:

- Analysis limited to high  $p_T$  prompt  $J/\psi$  only
- Feed down either neglected or subtracted, assumes that the shape of the  $\chi_c$  and  $\psi'$  distributions same as  $J/\psi$
- No comparison to fixed-target total cross sections
- No attempt to determine how matrix elements depend on quark mass or scale

# Global Analysis I: PHENIX at RHIC and CDF at the Tevatron

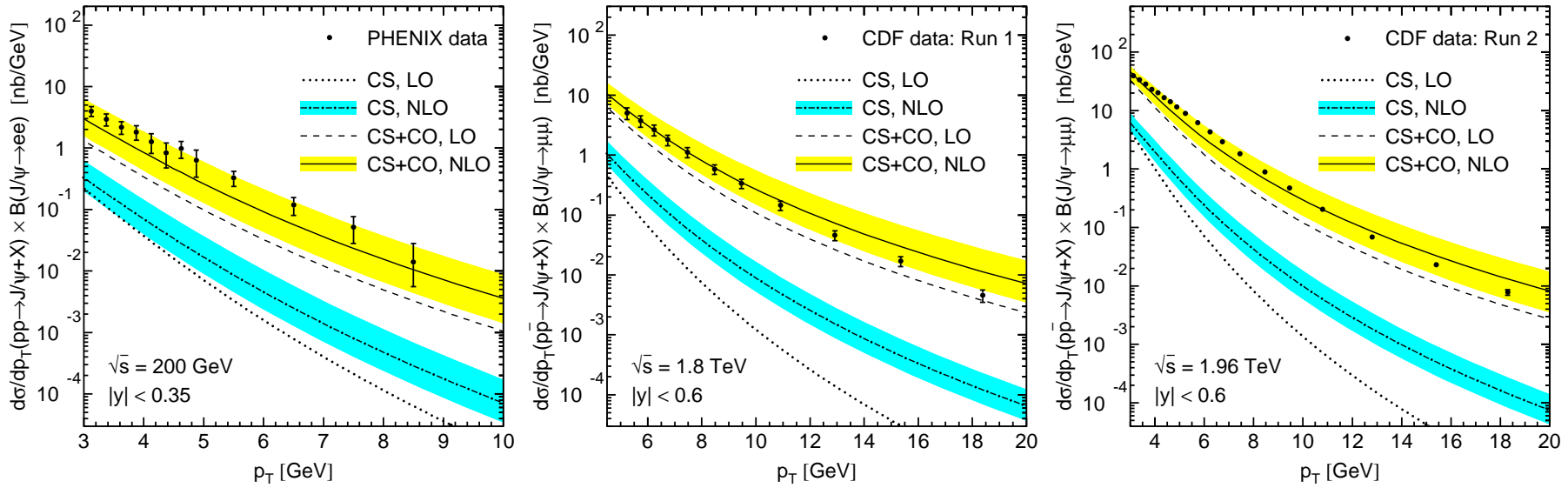


Figure 12: NLO NRQCD fit compared to the PHENIX (RHIC,  $\sqrt{s} = 200$  GeV) and CDF (Tevatron,  $\sqrt{s} = 1.96$  TeV) data.

# Global Analysis II: LHCb at 7 TeV

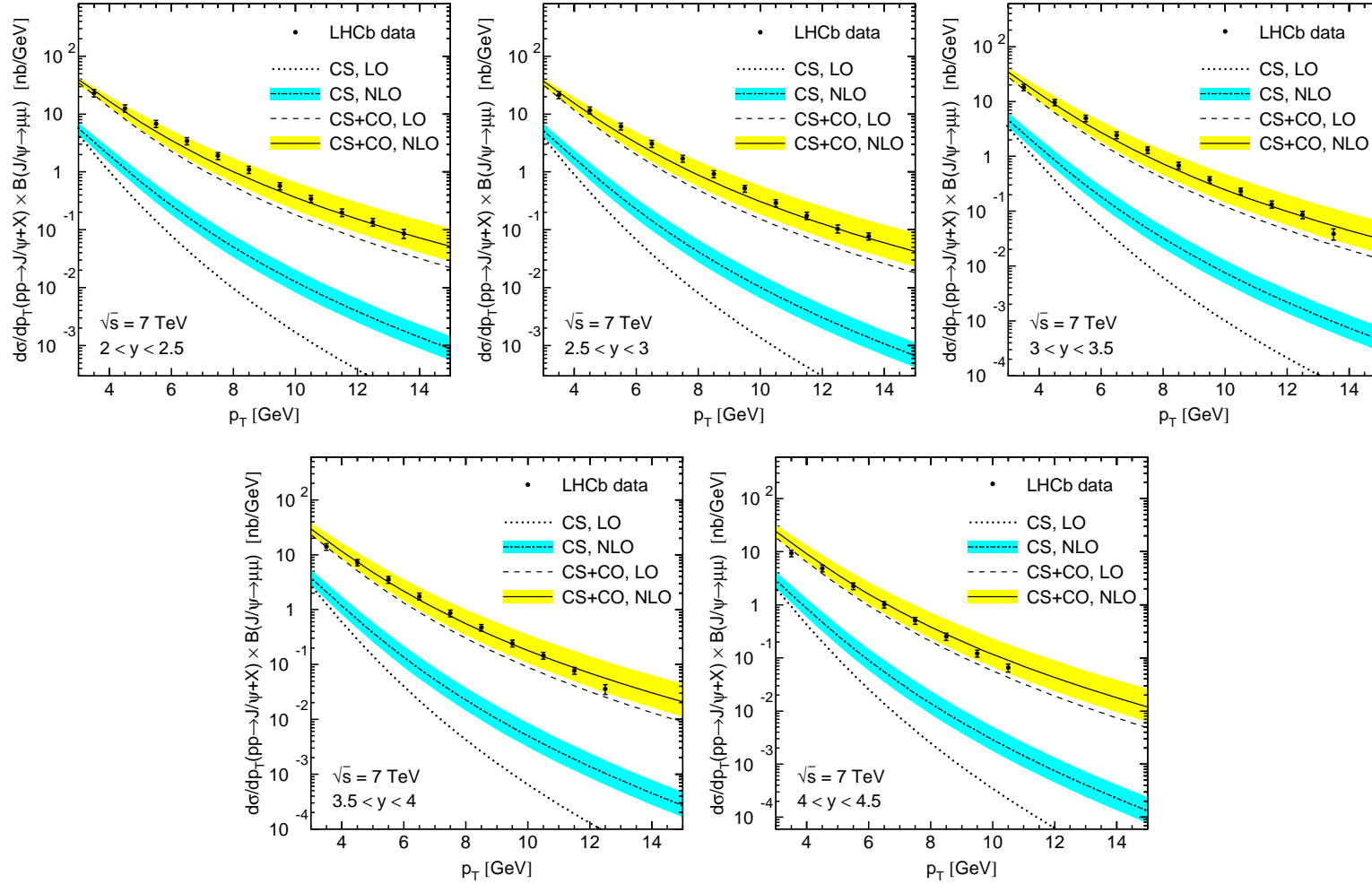


Figure 13: NLO NRQCD fit compared to LHCb data (LHC,  $\sqrt{s} = 7$  TeV, best available  $J/\psi$  data so far at the LHC).

# Global Analysis III: H1 at HERA

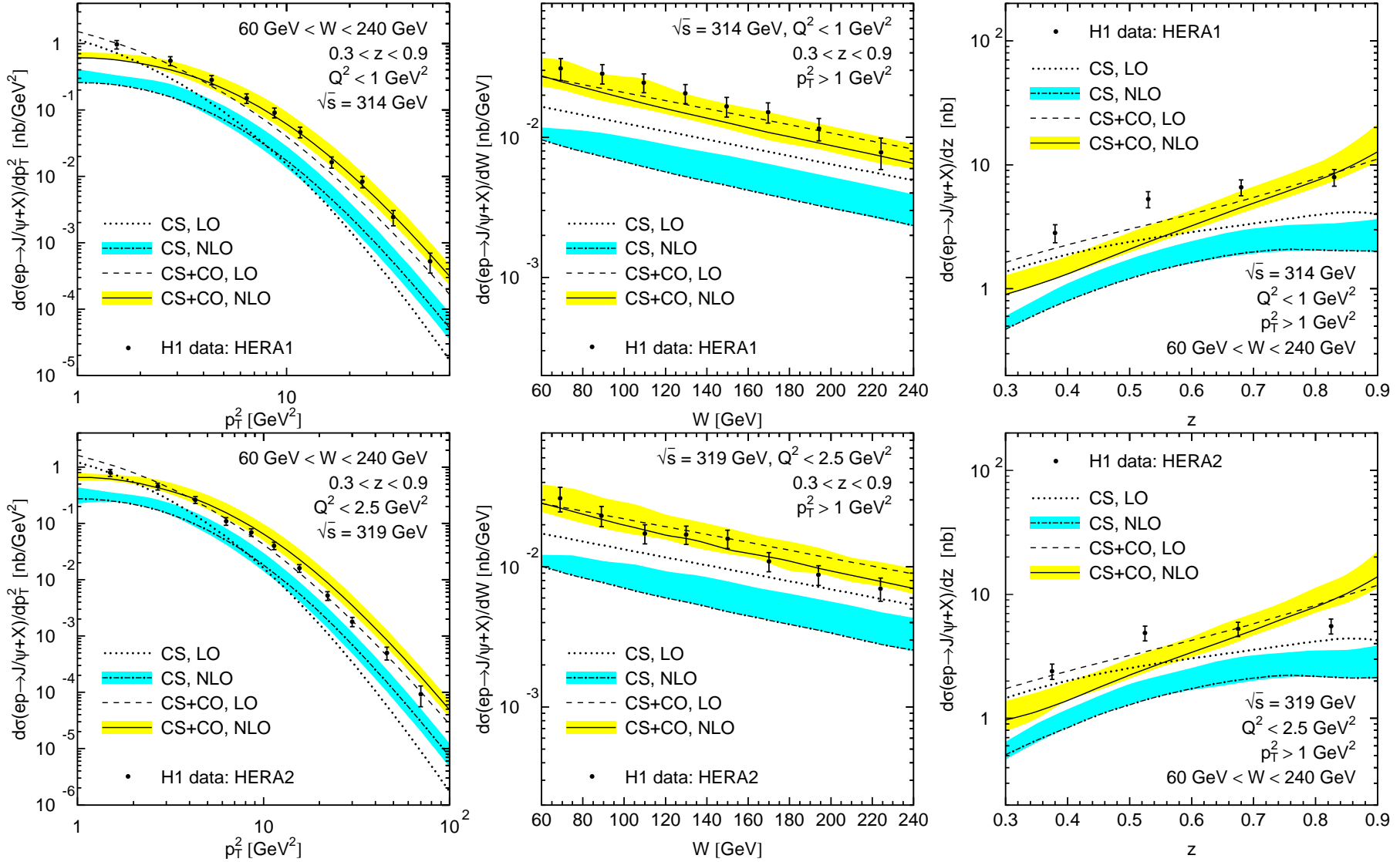


Figure 14: NLO NRQCD fit compared to H1 (HERA,  $ep$ ) data.

# Polarization Crucial Test of Production Models

At large  $p_T$ , the dominant mechanism of quarkonium production is gluon fragmentation into a color octet  $Q\bar{Q}$  ( $c\bar{c}[{}^3S_1^{(8)}]$ )

Fragmenting gluon is nearly on mass shell and thus transversely polarized, polarization should be retained during hadronization even though diluted by radiative corrections, color singlet production and feed down

$\alpha = (\sigma_T - 2\sigma_L)/(\sigma_T + 2\sigma_L)$ :  $\alpha = 0$ , no polarization;  $\alpha = 1$ , transverse polarization;  $\alpha = -1$ , longitudinal polarization

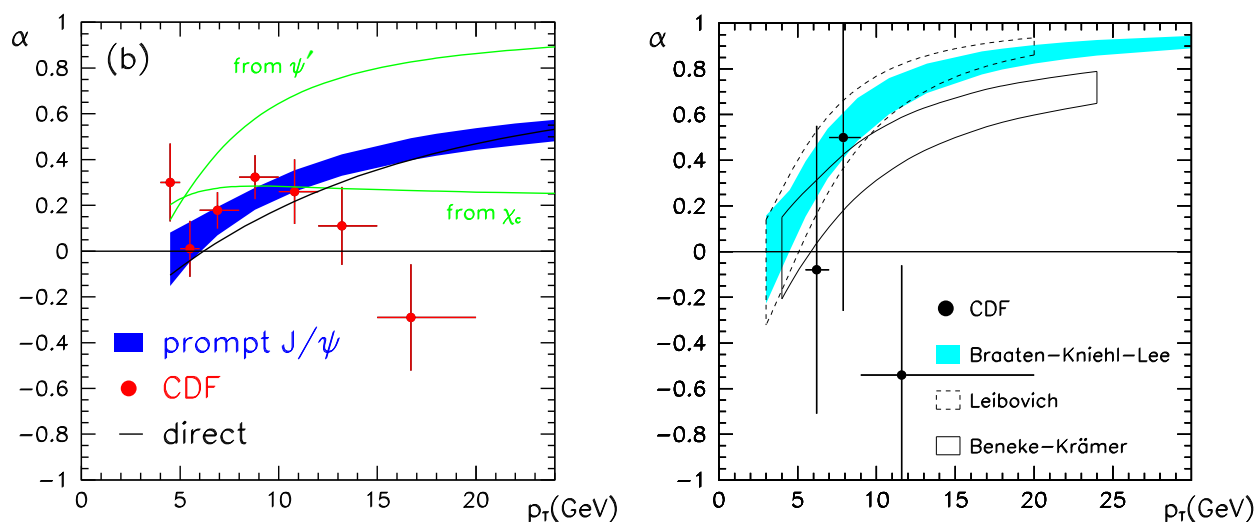


Figure 15: Left-hand side:  $J/\psi$  polarization at the Tevatron. The band is the total NRQCD-factorization prediction. The other curves give the contributions from feed down from higher charmonium states. Right-hand side:  $\psi'$  polarization at the Tevatron. The bands give various NRQCD-factorization predictions. The data points are from the CDF measurement [Phys. Rev. Lett. **85** (2000) 2886]. From Braaten *et al.*, Phys Rev. D **62** (2000) 094005.

# $\Upsilon$ Polarization Still Needs Work

$\Upsilon$  should work better because it is heavier, velocity and  $\alpha_s$  expansions should both be better under control

CDF and D0 polarization measurements disagree sharply – CDF: no polarization for  $p_T < 15$  GeV,  $\alpha \rightarrow -1$  at high  $p_T$ ; D0:  $\alpha$  negative at low  $p_T$ , positive at high  $p_T$

Both measurements inconsistent with predictions although feed down is more of a problem for  $\Upsilon(1S)$  than for  $J/\psi$

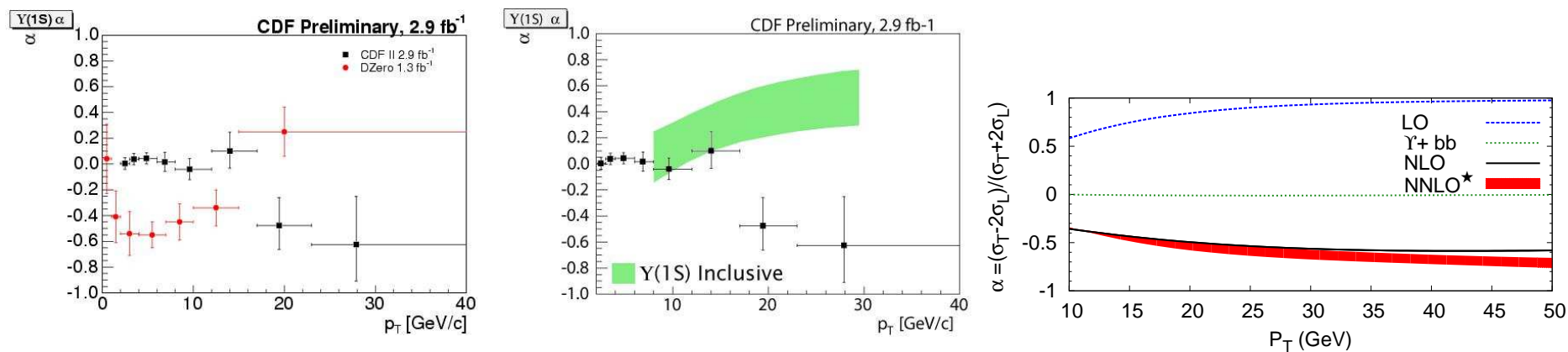


Figure 16: Left:  $\Upsilon(1S)$  polarization data from CDF (black) and D0 (red) in  $\sqrt{s} = 1.96$  TeV  $p\bar{p}$  collisions at the Tevatron. Center: Comparison with LO NRQCD calculation. Right: Calculation of polarization in CSM, note that LO CSM is transversely polarized, switches to longitudinal polarization at higher order.

# Polarization Results from Global Analysis

Polarized cross section,  $W \approx 1 + \lambda_\theta \cos^2 \theta$  with  $\lambda_\theta = 1$ , transverse polarization; 0, no polarization;  $-1$ , longitudinal polarization

Results shown in helicity frame, LO CSM and NRQCD calculations give transverse polarization, NLO CSM gives longitudinal polarization

Neither gives good description of Tevatron and ALICE data so far

Frame dependence is significant, soon CMS analysis will come out – lots of recent work by Faccioli, Lourenco, Seixas, Wohri in this area

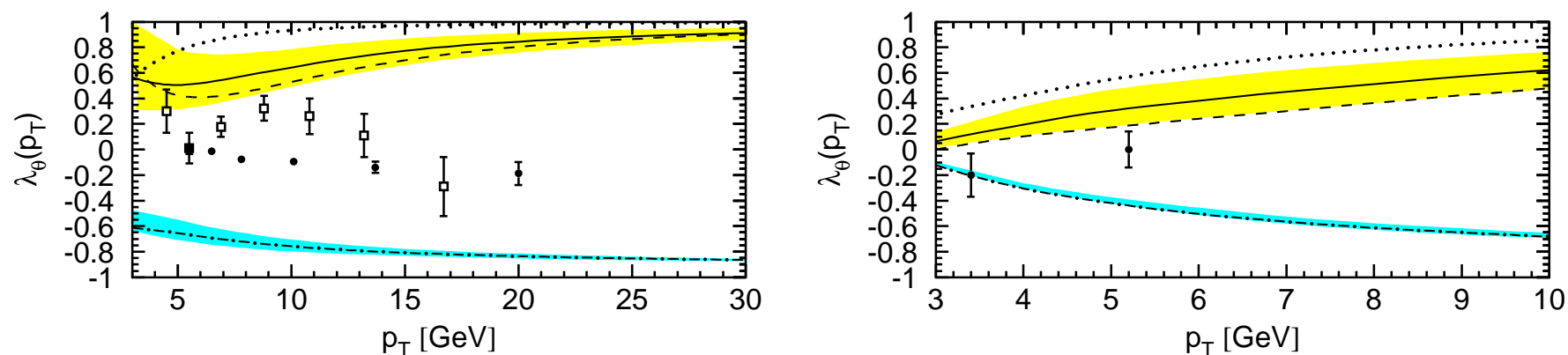


Figure 17: The  $J/\psi$  polarization at the Tevatron (left) and at ALICE (right) compared to LO CSM (dotted); NLO CSM (cyan dot-dashed), LO NRQCD (dashed), NLO NRQCD (yellow solid).

# Production By Intrinsic Charm

Intrinsic Charm –  $c\bar{c}$  pairs in the hadron wavefunction liberated by soft interactions  
– has been around a long time (Brodsky *et al.*)

Charm production seems to be anomalously large at high momentum fractions

- EMC  $F_2^c$  large at higher  $x$  and  $Q^2$
- Leading charm asymmetries in hadroproduction
- Large  $pp \rightarrow \Lambda_c X$  production cross section at  $x_F > 0.5$  (ISR)
- Double  $J/\psi$  production at high  $x_F$  in hadroproduction

EMC (EMC, Hoffmann and Moore) result confirmed with NLO calculation of both extrinsic (gluon that splits to  $c\bar{c}$  couples to single valence quark in hadron) and intrinsic charm (Harris, Smith and R.V., Nucl. Phys. B461 (1996) 181)

HERA data on  $F_2^c$  is at too low  $x$  to check EMC measurement

# Intrinsic Charm

Proton wavefunction can be expanded as sum over complete basis of quark and gluon states:  $|\Psi_p\rangle = \sum_m |m\rangle \psi_{m/p}(x_i, k_{T,i}, \lambda_i)$

$|m\rangle$  are color singlet state fluctuations into Fock components  $|uud\rangle, |uudg\rangle \cdots |uudc\bar{c}\rangle$

Boost invariant wavefunctions  $\psi_{m/p}(x_i, k_{T,i}, \lambda_i)$  depend on  $x_i = k_i^+/P^+$  and  $k_{T,i}$  the momentum fraction and transverse momentum for each parton. Momentum conservation demands  $\sum_{i=1}^n x_i = 1$  and  $\sum_{i=1}^n \vec{k}_{T,i} = 0$ , where  $n$  is the number of partons in Fock state  $|m\rangle$

The intrinsic charm fluctuations can be freed by a soft interaction if the system is probed during the time  $\Delta t = 2p_{\text{lab}}/M_{c\bar{c}}^2$  that the fluctuations exist

Dominant Fock state configurations have minimal invariant mass,  $M^2 = \sum_i m_{T,i}^2/x_i$ , where  $m_{T,i}^2 = k_{T,i}^2 + m_i^2$  is the squared transverse mass of parton  $i$  in the state; corresponds to configurations with equal rapidity constituents

Since intrinsic charm quarks have the same rapidity as other partons in the state, their larger mass gives them a higher momentum fraction than the comoving light partons

# Light Cone Intrinsic Charm Quark Distribution

Frame-independent Fock state wavefunction

$$\Psi(\vec{k}_{\perp i}, x_i) = \frac{\Gamma(\vec{k}_{\perp i}, x_i)}{m_h^2 - M^2}$$

Vertex function  $\Gamma$  assumed to be slowly varying so the denominator controls the particle distributions; mean  $k_T^2$  used to calculate the  $x$  distributions

Probability distribution for  $n$ -particle Fock state as a function of  $x$

$$\frac{dP_{ic}}{dx_i \cdots dx_n} = N_n [\alpha_s^2(M_{c\bar{c}})]^2 \frac{\delta(1 - \sum_{i=1}^n x_i)}{(m_h^2 - \sum_{i=1}^n (\widehat{m}_i^2/x_i))^2}$$

$N_n$  is a normalization to total probability for each state; heavy quark limit,  $\widehat{m}_c, \widehat{m}_{\bar{c}} \gg m_h, \widehat{m}_q$

$$\frac{dP_{ic}}{dx_i \cdots dx_n} = N_n [\alpha_s^2(M_{c\bar{c}})]^2 \frac{x_c x_{\bar{c}}}{(x_c + x_{\bar{c}})^2} \delta(1 - \sum_{i=1}^n x_i)$$

Finally, in a  $|uudc\bar{c}\rangle$  state,  $n = 5$  and integration over light quarks and  $\bar{c}$  gives

$$c(x) \propto \frac{dP_{ic}(x)}{dx} = \frac{1}{2} N_5 x^2 \left[ \frac{1}{3} (1-x)(1+10x+x^2) + 2x(1+x) \ln x \right]$$

If the intrinsic charm probability is 1%,  $N_5 = 36$

Structure function,  $F_2^c$ , related to charm quark distribution by  $F_2^c = \frac{8}{9} x c(x)$  at leading order with no mass effects

# Global Analysis with Intrinsic Charm by Pumplin *et al.*

Performed global analysis including the presence of nonperturbative charm in the parton densities

Pumplin *et al.* refer to extrinsic charm as *radiatively generated charm*, the charm parton density is completely determined by the gluon and light quark parameters and evolution

Their work is first general global analysis to include: coherent treatment of nonzero quark masses in pQCD and experimental inputs that constrain the charm degree of freedom (they use HERA data, not EMC data)

Compare three different scenarios:

- Light cone formalism of Brodsky *et al.*

$$c(x) = \bar{c}(x) = Ax^2[6x(1+x)\ln x + (1-x)(1+10x+x^2)]$$

- Meson cloud picture with  $c(x) \neq \bar{c}(x)$

$$c(x) = Ax^{1.897}(1-x)^{6.095}$$

$$\bar{c}(x) = \bar{A}x^{2.511}(1-x)^{4.929}$$

$$0 = \int_0^1 dx [c(x) - \bar{c}(x)]$$

- Charm distribution is sea-like, similar to light flavor sea

$$c(x) = \bar{c}(x) \propto \bar{d}(x) + \bar{u}(x)$$

# Extracted Charm Quark Distributions Differ Significantly

Extracted Brodsky *et al.* result is similar to that obtained by Harris *et al.* without incorporating a global analysis

Meson cloud IC gives harder distribution for the  $\Lambda_c$ -like charm quark than the  $\bar{D}$  meson anticharm quark

Sea-like IC results in an enhancement over all  $x$

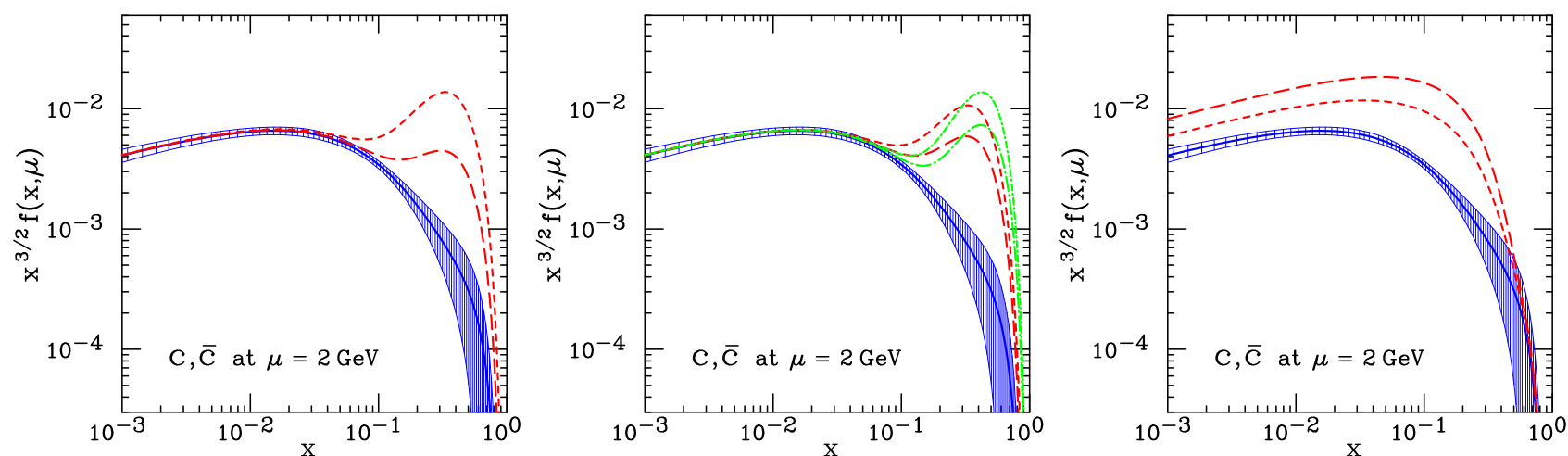


Figure 18: The three IC scenarios at scale  $\mu = 2$  GeV. The left-hand panel shows the Brodsky *et al.* light-cone result; the central shows the meson cloud result (the baryonic component is that with the peak at higher  $\langle x \rangle_{c+\bar{c}}$ ); and the right panel shows the sea-like IC shape. The long-dashed and short dashed curves correspond to the minimum and maximum values of  $\langle x \rangle_{c+\bar{c}}$  in each scenario. The solid curve and shaded region show the central value and uncertainty from CTEQ6.5, which contains no IC. [From Pumplin *et al.*]

# Scale Evolution of Charm Distribution

QCD evolution makes charm distribution softer at higher scales

IC component is dominant at large  $x$  and remains different from evolution without IC, even at large scales

Scale of  $x$  axis is linear in  $x^{1/3}$  to enhance large  $x$  region

IC should have observable consequences in experiments that can access the large  $x$  region

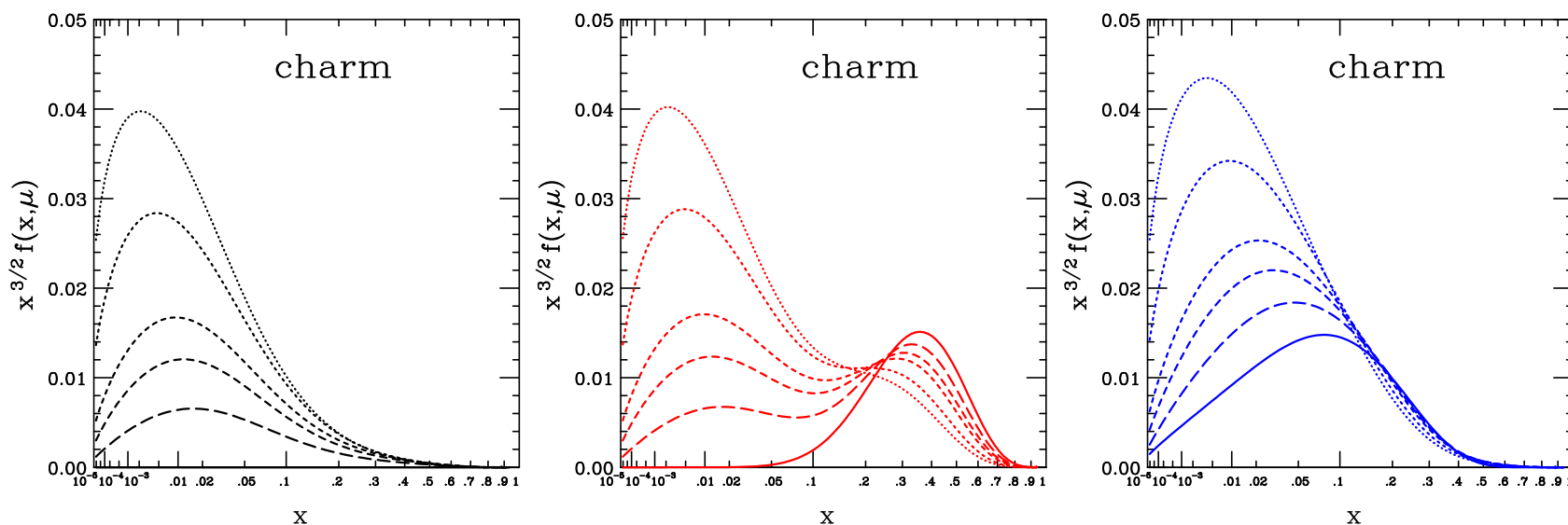


Figure 19: The scale evolution of the charm distribution without IC (left); with the Brodsky *et al.* light-cone result (center); and the sea-like IC shape (right). The results are shown for  $\mu = 1.3$  (solid), 2, 3.16, 5, 20 and 100 (dotted) GeV in each case. [From Pumplin *et al.*]

# Possible Observable Consequences for $J/\psi$ at RHIC

Brodsky and Lansberg computed CSM quarkonium rapidity distribution at LO and NLO

Also included a LO contribution due to  $cg \rightarrow J/\psi c$  enhanced by IC, diagram (b) below

Such an additional  $J/\psi$  production mechanism could be observed via a charm jet opposite in azimuth to the  $J/\psi$

Azimuthal correlation would be sensitive to the charm distribution in the proton

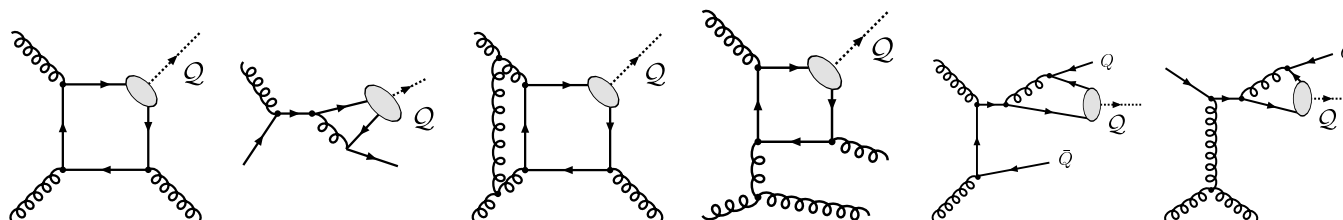


Figure 20: Representative diagrams contributing to  $^3S_1$  quarkonium (denoted  $Q$ ) hadroproduction via color singlet channels at order  $\alpha_s^3$  (a,b) and  $\alpha_s^4$  (c,d,e,f). The quark and antiquark attached to the ellipses are assumed to be on shell with zero relative velocity  $v$ .

# PHENIX Results Compared to CSM (+ IC)

Brodsky and Lansberg calculated direct  $J/\psi$  (no  $\chi_c$  or  $\psi'$  feed down) in the LO ( $\mathcal{O}(\alpha_s^3)$ ) and NLO (up to  $\mathcal{O}(\alpha_s^4)$ ) CSM

Obtained uncertainty bands by varying charm quark mass and scale

NLO CSM in agreement with lower bound of PHENIX  $J/\psi$  data

Including  $cg$  diagrams with sea-like IC improves agreement;  $J/\psi + c$  final state is significant fraction of total  $J/\psi$

Light cone IC shape out of reach of current PHENIX setup

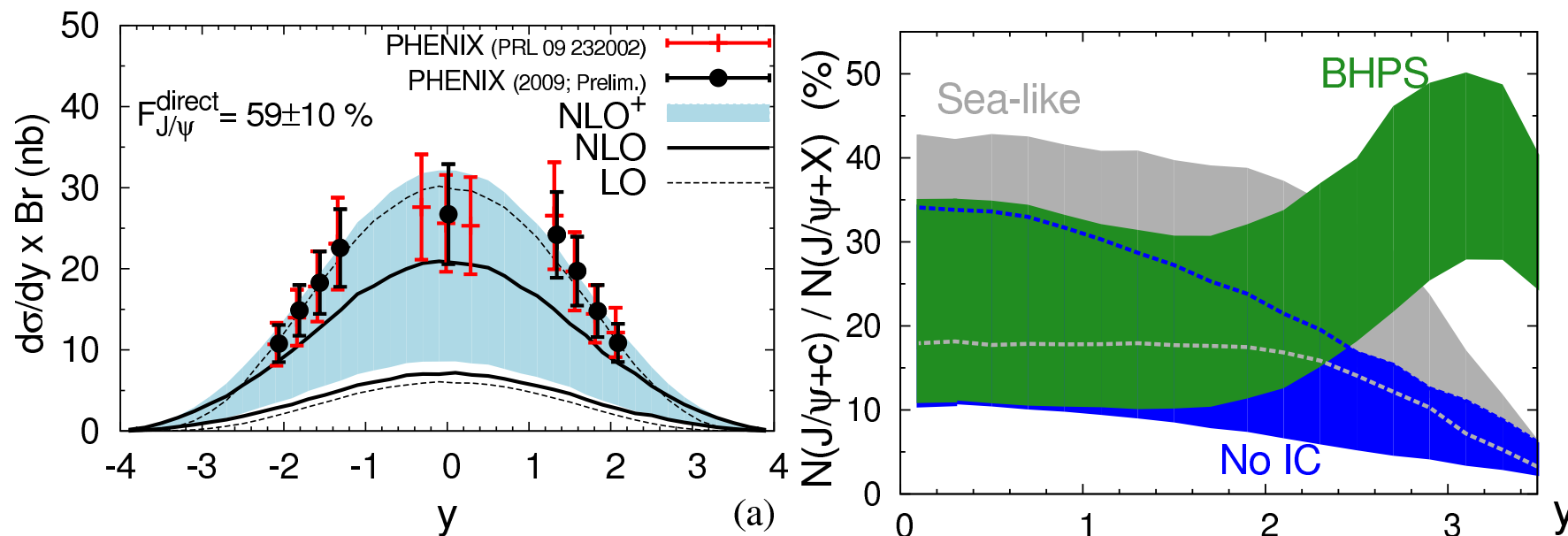


Figure 21: (Left) The rapidity distribution,  $Bd\sigma_{J/\psi}^{direct}/dy$  from PHENIX multiplied by the fraction of direct  $J/\psi$  production compared to the CSM at LO ( $\alpha_s^3$ ) by  $gg$  fusion only (thin-dashed lines), at NLO (up to  $\alpha_s^4$ ) by  $gg$  and  $qg$  fusion only (thick-solid lines) and the sum “NLO +  $cg$  fusion” with the sea-like IC, denoted NLO+ (light-blue band). (Right) Fraction of  $J/\psi$  produced in association with a single  $c$ -quark ( $gc \rightarrow J/\psi c$ ) relative to the direct yield (NLO+) as a function of  $y_\psi$  and for no IC, sea-like and Brodsky *et al.* (BHPS).

# Color Evaporation Model

All quarkonium states are treated like  $Q\bar{Q}$  ( $Q = c, b$ ) below  $H\bar{H}$  ( $H = D, B$ ) threshold

Distributions for all quarkonium family members similar, modulo decay feed down, production ratios should be independent of  $\sqrt{s}$

At LO,  $gg \rightarrow Q\bar{Q}$  and  $q\bar{q} \rightarrow Q\bar{Q}$ ; NLO add  $gq \rightarrow Q\bar{Q}q$

$$\sigma_Q^{\text{CEM}} = F_Q \sum_{i,j} \int_{4m_Q^2}^{4m_H^2} d\hat{s} \int dx_1 dx_2 f_{i/p}(x_1, \mu^2) f_{j/p}(x_2, \mu^2) \hat{\sigma}_{ij}(\hat{s}) \delta(\hat{s} - x_1 x_2 s)$$

Values of  $m_Q$  and  $Q^2$  fixed from NLO calculation of  $Q\bar{Q}$  production

Main uncertainties arise from choice of PDFs, heavy quark mass, renormalization ( $\alpha_s$ ) and factorization (evolution of PDFs) scales

Inclusive  $F_Q$  fixed by comparison of NLO calculation of  $\sigma_Q^{\text{CEM}}$  to  $\sqrt{s}$  dependence of  $J/\psi$  and  $\Upsilon$  cross sections,  $\sigma(x_F > 0)$  and  $Bd\sigma/dy|_{y=0}$  for  $J/\psi$ ,  $Bd\sigma/dy|_{y=0}$  for  $\Upsilon$

Data and branching ratios used to separate the  $F_Q$ 's for each quarkonium state

Resonance	$J/\psi$	$\psi'$	$\chi_{c1}$	$\chi_{c2}$	$\Upsilon$	$\Upsilon'$	$\Upsilon''$	$\chi_b(1P)$	$\chi_b(2P)$
$\sigma_i^{\text{dir}}/\sigma_H$	0.62	0.14	0.6	0.99	0.52	0.33	0.20	1.08	0.84
$f_i$	0.62	0.08	0.16	0.14	0.52	0.10	0.02	0.26	0.10

Table 2: The ratios of the direct quarkonium production cross sections,  $\sigma_i^{\text{dir}}$ , to the inclusive  $J/\psi$  and  $\Upsilon$  cross sections, denoted  $\sigma_H$ , and the feed down contributions of all states to the  $J/\psi$  and  $\Upsilon$  cross sections,  $f_i$ , Digal *et al.*

# Why CEM?

Open and hidden charm photo- and hadroproduction show similar energy dependence

High  $p_T$  Tevatron Run I data show that, within uncertainties of the data, the prompt  $J/\psi$ , the  $\psi'$  and  $\chi_c$   $p_T$  dependencies are the same

Amundsen *et al.* calculated partial  $p_T$  distribution (only real part) harder than data at high  $p_T$ , undershoots at low  $p_T$  – likely because they do not include any  $k_T$  smearing

Gavai *et al.* calculated complete  $J/\psi$   $p_T$  distribution starting from exclusive NLO  $Q\bar{Q}$  production code by Mangano *et al.*

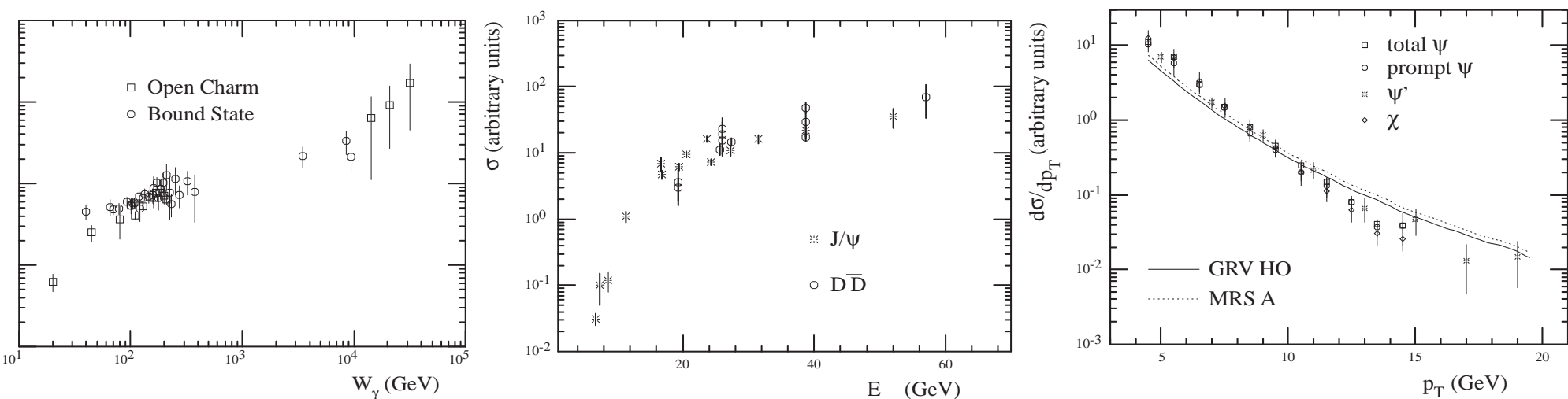


Figure 22: (Left) Photoproduction data as a function of the photon energy in the hadron rest frame,  $W_\gamma$ . (Center) Hadroproduction data as a function of the center-of-mass energy,  $E_{cm}$ . In both cases, the normalization has been adjusted to show the similar shapes of the data. (Right) Run I data from the CDF Collaboration, shown with arbitrary normalization. The curves are the predictions of the color evaporation model at tree level, also shown with arbitrary normalization. [Amundson *et al.*]

# Total Cross Sections

Partonic total cross section only depends on quark mass  $m$ , not kinematics  
To NLO

$$\hat{\sigma}_{ij}(s, m, \mu_F^2, \mu_R^2) = \frac{\alpha_s^2(\mu_R^2)}{m^2} \left\{ f_{ij}^{(0,0)}(\rho) + 4\pi\alpha_s(\mu_R^2) \left[ f_{ij}^{(1,0)}(\rho) + f_{ij}^{(1,1)}(\rho) \ln(\mu_F^2/m^2) \right] + \mathcal{O}(\alpha_s^2) \right\}$$

$\rho = 4m^2/s$ ,  $s$  is partonic center of mass energy squared

$\mu_F$  is factorization scale, separates hard part from nonperturbative part

$\mu_R$  is renormalization scale, scale at which strong coupling constant  $\alpha_s$  is evaluated

$\mu_F = \mu_R$  in evaluations of parton densities

$f_{ij}^{(a,b)}$  are dimensionless,  $\mu$ -independent scaling functions,  $a = 0, b = 0$  and  $ij = q\bar{q}, gg$  for LO,  $a = 1, b = 0, 1$  and  $ij = q\bar{q}, gg$  and  $qg, \bar{q}g$  for NLO

$f_{ij}^{(0,0)}$  are always positive,  $f_{ij}^{(1,b)}$  can be negative also

Note that if  $\mu_F^2 = m^2$ ,  $f_{ij}^{(1,1)}$  does not contribute

# Scaling Functions to NLO

Near threshold,  $\sqrt{s}/2m \rightarrow 1$ , Born contribution is large but dies away for  $\sqrt{s}/2m \rightarrow \infty$

At large  $\sqrt{s}/2m$ ,  $gg$  channel is dominant, then  $qg$

**NLO  $gg$  and  $qg$  scaling functions independent of energy at  $\sqrt{s}/2m > 20$**

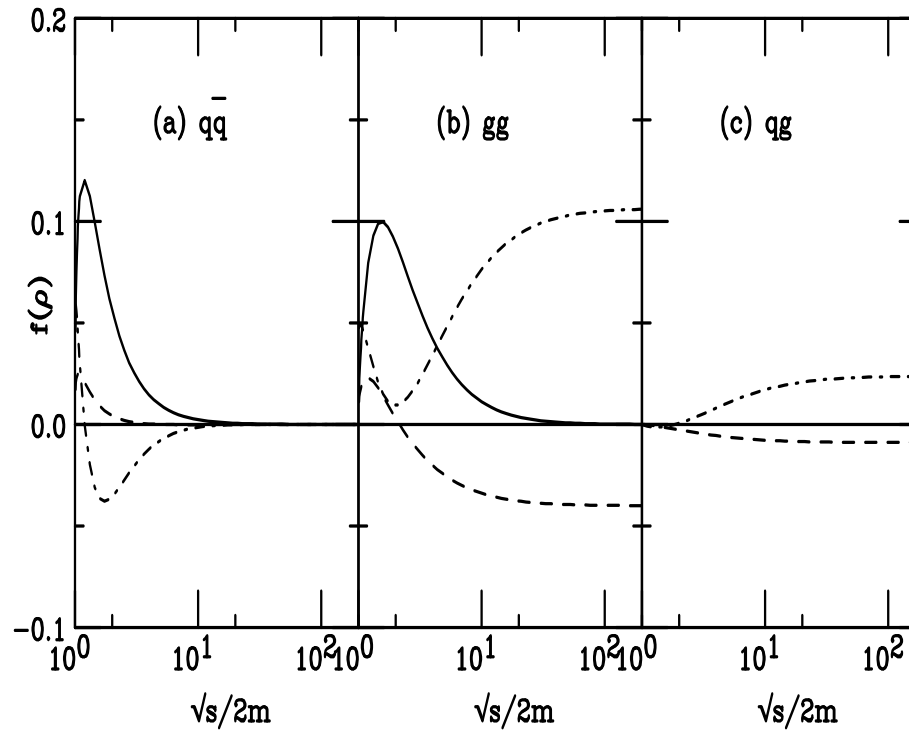


Figure 23: Scaling functions needed to calculate the total partonic  $Q\bar{Q}$  cross section. The solid curves are the Born results,  $f_{ij}^{(0,0)}$ , the dashed and dot-dashed curves are NLO contributions,  $f_{ij}^{(1,1)}$  and  $f_{ij}^{(1,0)}$  respectively.

# Some Diagrams Contributing to NLO Heavy Flavor Production

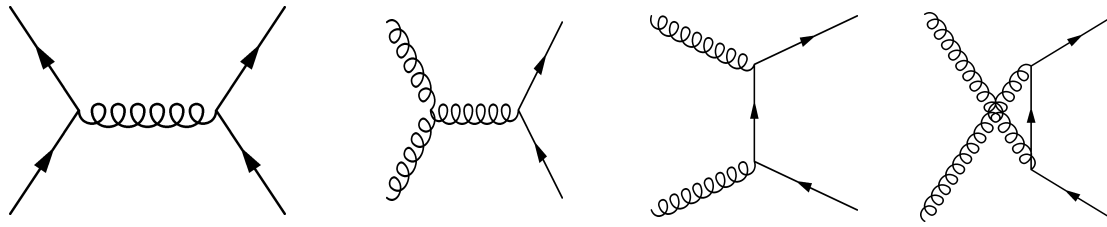


Figure 24: Leading order processes contributing to  $Q\bar{Q}$  production.

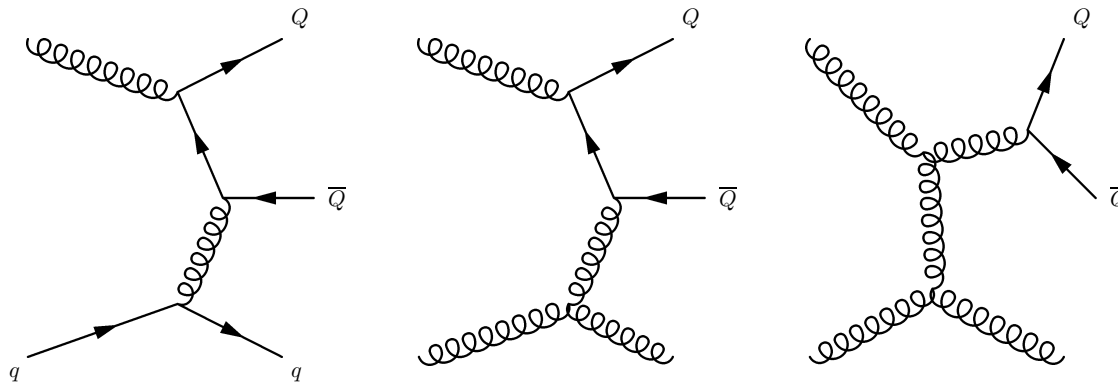


Figure 25: Examples of next-to-leading order diagrams contributing to  $Q\bar{Q}$  production:  $qg \rightarrow qQ\bar{Q}$  (left) and  $gg \rightarrow Q\bar{Q}g$  (middle and right).

# Determining the Uncertainty on the CEM Result

Previously took 'by eye' fit to  $Q\bar{Q}$  total cross section

Dates back to original Hard Probes Collaboration report in 1995 – only PDFs changed over time

Results shown here based on: first – using FONLL parameters for quark mass and scale; second – fitting mass and scale parameters at NLO to total charm cross section data and using same parameters to calculate  $J/\psi$  in CEM

One final remark: there is no calculation of the polarization, would need to start from NLO polarized  $Q\bar{Q}$  production calculation

BTW, no prediction does not necessarily mean a flat distribution, it means there is no calculation

Work reported here done in collaboration with Randy Nelson (UCD and LLNL) and Tony Frawley (FSU)

# Choosing $J/\psi$ Parameters I: FONLL Fiducial Set

Main sources of uncertainty:

Mass:  $1.3 < m < 1.7$  GeV for charm (central value, 1.5 GeV)

Scale: renormalization,  $\mu_R$ , and factorization,  $\mu_F$ , scales governing  $\alpha_s$  and PDF behavior respectively

Parton Density: evolution of gluon density

With a given PDF set define a fiducial region of mass and scale that should encompass the true value:

- For  $\mu_F = \mu_R = m$ , vary mass between upper and lower end of range;
- For central mass value, vary scales independently within a factor of two:  
 $(\mu_F/m, \mu_R/m) = (1, 1), (2, 2), (0.5, 0.5), (0.5, 1), (1, 0.5), (1, 2), (2, 1)$ .

Define upper and lower bounds of theoretical values; the maximum and minimum may not come from the same set of parameters at a given energy or  $p_T$

The uncertainty band comes from the upper and lower limits of mass and scale uncertainties added in quadrature:

$$\sigma_{\max} = \sigma_{\text{cent}} + \sqrt{(\sigma_{\mu, \max} - \sigma_{\text{cent}})^2 + (\sigma_{m, \max} - \sigma_{\text{cent}})^2}$$

$$\sigma_{\min} = \sigma_{\text{cent}} - \sqrt{(\sigma_{\mu, \min} - \sigma_{\text{cent}})^2 + (\sigma_{m, \min} - \sigma_{\text{cent}})^2}$$

# Main Sources of Uncertainty

$\alpha_s$  changing rapidly, especially for  $\mu_R = \mu_0/2$

Results depend on choice of  $\mu_0$  in parton densities (lower  $\mu_0$  means smaller  $\alpha_s$  at low scales)

Low factorization scales result in unreliable results for gluon densities

Backwards evolution required for low scale ( $\mu_F = m, m/2$ ) charm production

At RHIC energies and higher, the gluon distribution with  $\mu_F = m/2$  turns over while the distribution with  $\mu_F = m$  is almost independent of  $x$  for  $x < 0.01$

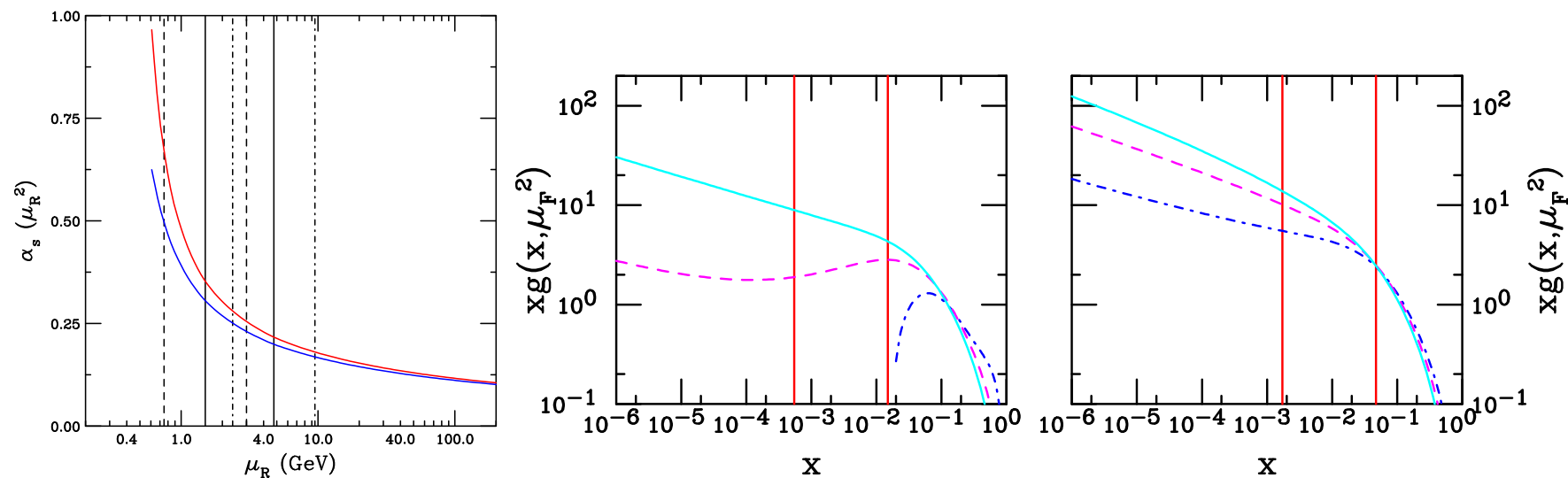


Figure 26: (Left) the running coupling constant for CTEQ6M (red) with  $\Lambda^{n_f=5} = 0.226$  GeV and for GRV98 (blue) with  $\Lambda^{n_f=5} = 0.1677$  GeV. The vertical bars are at  $\mu_R = 1.5$  and  $4.75$  GeV. (Right) The CTEQ6M parton densities as a function of  $x$  for  $\mu_F/m = 0.5$  (dot-dashed),  $\mu_F/m = 1$  (dashed) and  $\mu_F/m = 2$  (solid) for  $m = 1.5$  GeV (left-hand side) and  $4.75$  GeV (right-hand side). The vertical lines are at  $x = 2m/\sqrt{S}$  in  $\sqrt{S} = 200$  GeV and  $5.5$  TeV  $pp$  collisions at RHIC and the LHC.

# FONLL Calculation of $c\bar{c}$ Uncertainty

$c\bar{c}$  cross section dependence on  $\sqrt{s}$  with FONLL parameter sets (left), uncertainty band on  $c\bar{c}$  cross section (right)

None of the FONLL sets fit the data, large  $\chi^2/\text{dof}$

No convergence for  $\mu_R/m < 1$  (large  $\alpha_s$ )

Problems with backward evolution of PDFs for  $\mu_F/m \leq 1$  (near or below minimum scale of PDFs)

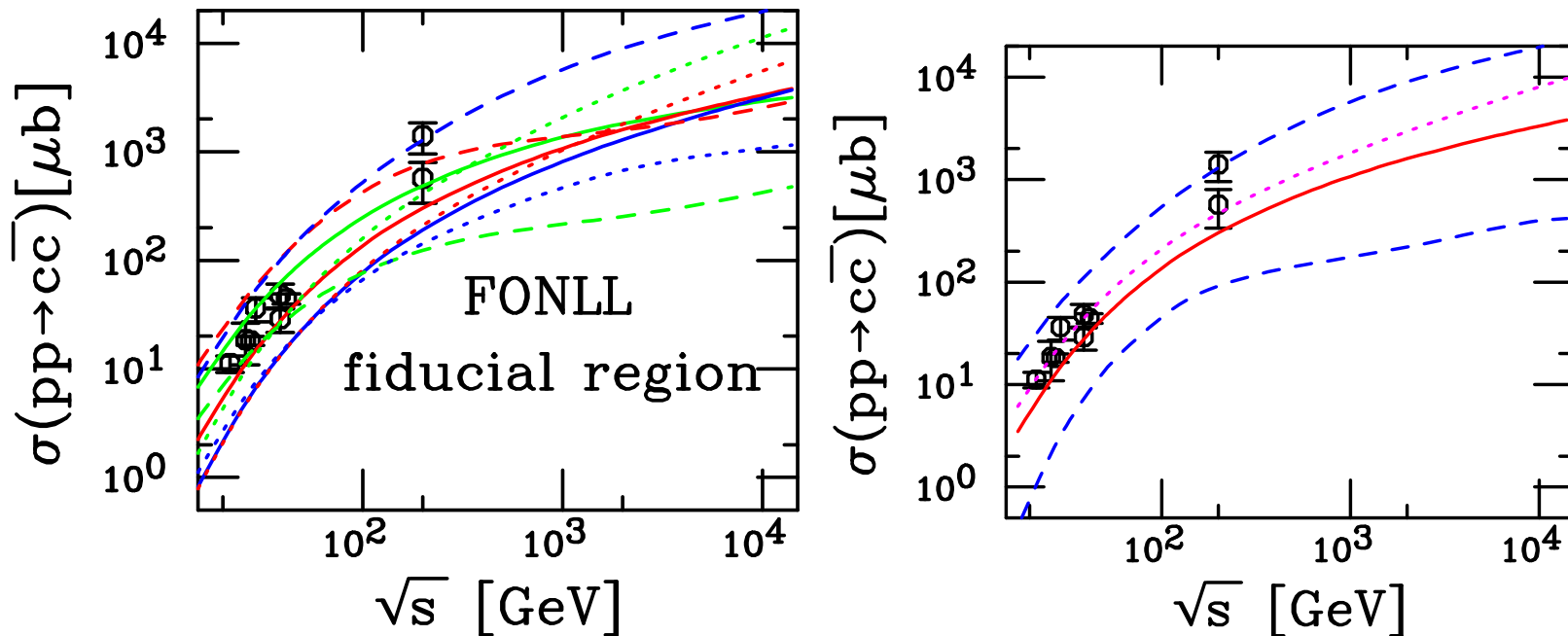


Figure 27: (Left) Total  $c\bar{c}$  cross sections calculated using CTEQ6M. The solid red curve is the central value  $(m, \mu_F/m, \mu_R/m) = (1.5 \text{ GeV}, 1, 1)$ . The green and blue solid curves are  $(1.3 \text{ GeV}, 1, 1)$  and  $(1.7 \text{ GeV}, 1, 1)$  respectively. The red, blue and green dashed curves correspond to  $(1.5 \text{ GeV}, 0.5, 0.5)$ ,  $(1.5 \text{ GeV}, 1, 0.5)$  and  $(1.5 \text{ GeV}, 0.5, 1)$  while the red, blue and green dotted curves are for  $(1.5 \text{ GeV}, 2, 2)$ ,  $(1.5 \text{ GeV}, 1, 2)$  and  $(1.5 \text{ GeV}, 2, 1)$ . (Right) Uncertainty band formed from adding mass and scale uncertainties in quadrature.

# $J/\psi$ Uncertainty Large, Can Only Define Upper Limit

Fit  $F_C$  CEM parameter for central mass and scale value, use same value for other calculations of fiducial range

At large  $\sqrt{s}$   $(\mu_F/m, \mu_R/m) = (0.5, 0.5)$ ,  $(0.5, 1)$  flattens because  $\mu_F < \mu_0$  of PDF

$m_c = 1.7$  GeV governs uncertainty at low  $\sqrt{s}$  since  $m_D/m_c \sim 1.1$ , small phase space for  $J/\psi$  production in CEM – doesn't make much sense

Large combination of mass and scale uncertainty makes lower limit ill defined

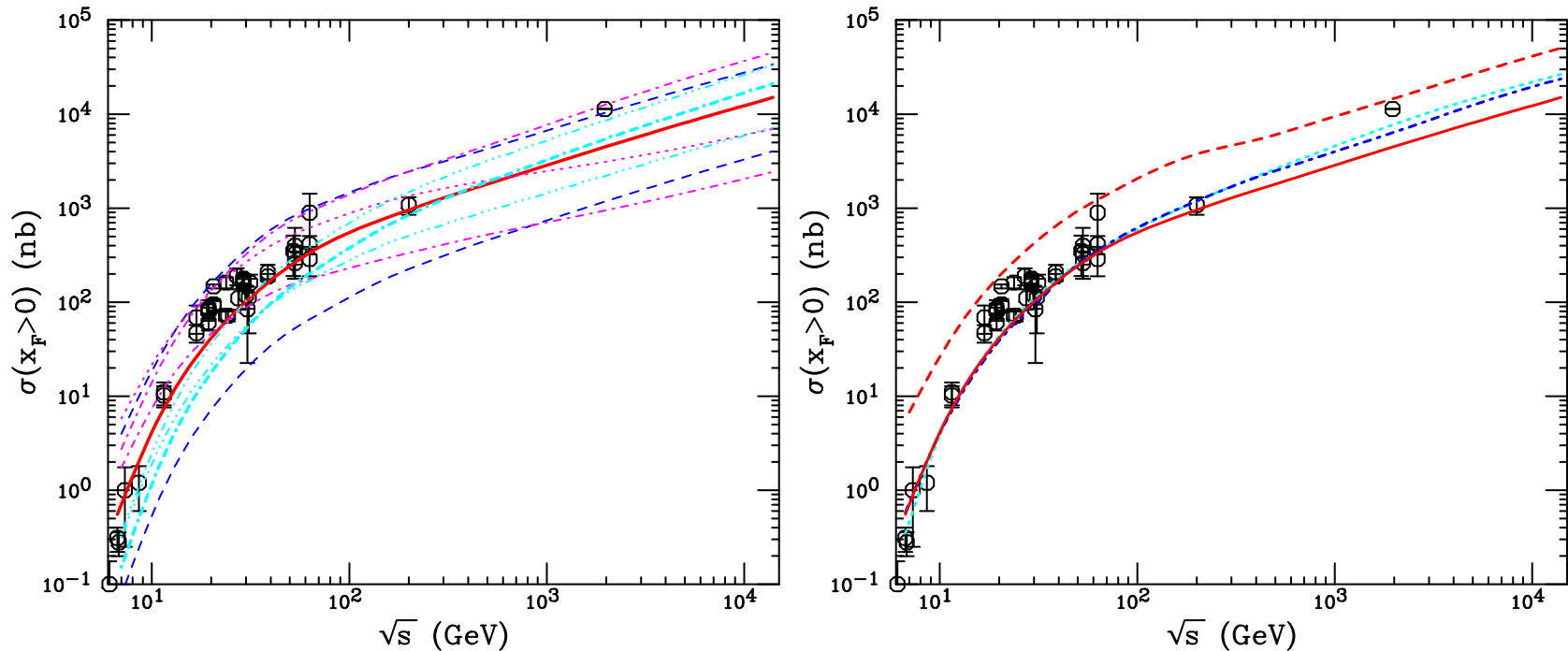


Figure 28: (Left) Total  $J/\psi$  cross sections calculated using CTEQ6M. The solid red curve is the central value  $(\mu_F/m, \mu_R/m) = (1, 1)$  with  $m = 1.5$  GeV. The upper and lower dashed blue curves are  $m = 1.3$  and  $1.7$  GeV with  $(1, 1)$  respectively. The dotted magenta curve corresponds to  $(0.5, 0.5)$  while the upper and lower magenta dot-dashed curves (above  $\sqrt{s} = 50$  GeV) correspond to  $(1, 0.5)$  and  $(0.5, 1)$ . The dash-dash-dotted cyan curve corresponds to  $(2, 2)$  while the upper and lower cyan dot-dot-dot-dashed curves (above  $\sqrt{s} = 50$  GeV) are  $(2, 1)$  and  $(1, 2)$ . The last 6 curves are all calculated for  $m_c = 1.5$  GeV. (Right) The solid and dashed red curves are the central value and upper limit for the  $J/\psi$  cross section. The solid and dashed red curves employ the MRST HO distributions while the dot-dashed blue curve is a result with CTEQ6M, both employing  $m_c = 1.2$  GeV,  $(\mu_F/m_T, \mu_R/m_T) = (2, 2)$ .

## Choosing $J/\psi$ Parameters II: Fitting $\sigma_{c\bar{c}}$

$J/\psi$  parameters based on fits to NLO total  $c\bar{c}$  cross section – caveat: full NNLO cross section unknown, could still be large correction

Employ  $m = 1.27$  GeV, value of charm quark mass from lattice calculations at  $m(3\text{ GeV})$

Use subset of  $c\bar{c}$  total cross section data to fix best fit values of  $\mu_F/m$  and  $\mu_R/m$

Result with  $\Delta\chi^2 = 1$  gives uncertainty on scale parameters;  $\Delta\chi^2 = 2.3$  gives one standard deviation on total cross section

Range of  $\mu_R$  for given  $m$  is very narrow; range of  $\mu_F$  is rather broad, especially when RHIC cross sections are included

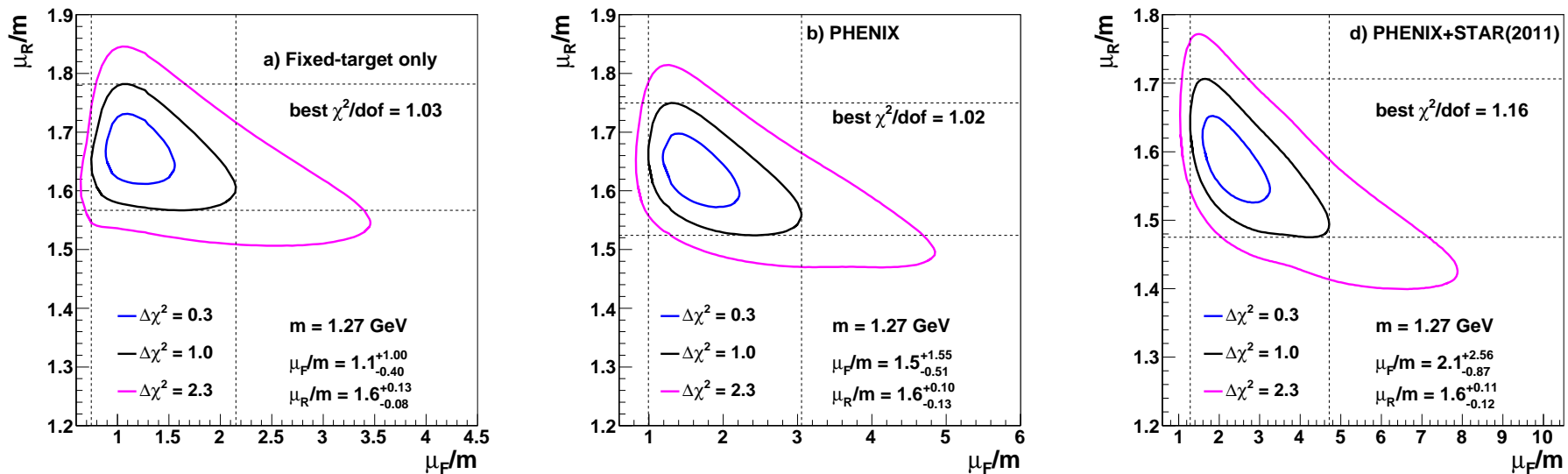


Figure 29: The  $\chi^2/\text{dof}$  contours for (left) fixed target data only, (center) including the PHENIX 200 GeV cross section, and (right) including the STAR 2011 cross section but excluding the STAR 2004 cross section. The best fit values are given for the furthest extent of the  $\Delta\chi^2 = 1$  contours.

# Energy Dependence of Fit Results

Fixed-target only fit (left) gives worst agreement with RHIC data and largest spread in total cross section (due to low factorization scales in fit region)

Including most recent STAR analysis with PHENIX data at  $\sqrt{s} = 200$  GeV gives strongest energy dependence and narrowest uncertainty region (right) than with PHENIX alone (center)

Remainder of results shown with fit to fixed-target + PHENIX + STAR (2011) on right-hand side

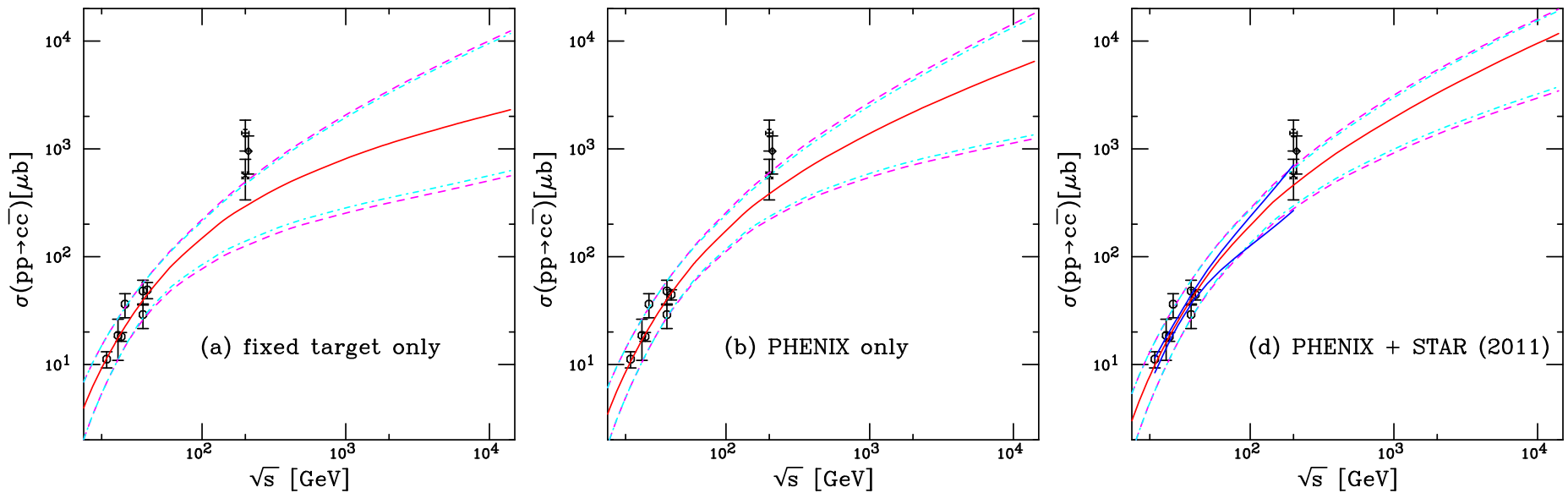


Figure 30: The energy dependence of the charm total cross section compared to data for (left) fixed target data only, (center) including the PHENIX 200 GeV cross section, and (right) including the STAR 2011 cross section but excluding the STAR 2004 cross section. The best fit values are given for the furthest extent of the  $\Delta\chi^2 = 1$  contours. The central value of the fit in each case is given by the solid red curve while the dashed magenta curves and dot-dashed cyan curves show the extent of the corresponding uncertainty bands. The dashed curves outline the most extreme limits of the band. On the bottom right, the solid blue curves in the range  $19.4 \leq \sqrt{s} \leq 200$  GeV represent the uncertainty obtained from the extent of the  $\Delta\chi^2 = 2.4$  contour of fit including STAR 2011 data.

# Uncertainty Due to Gluon Densities

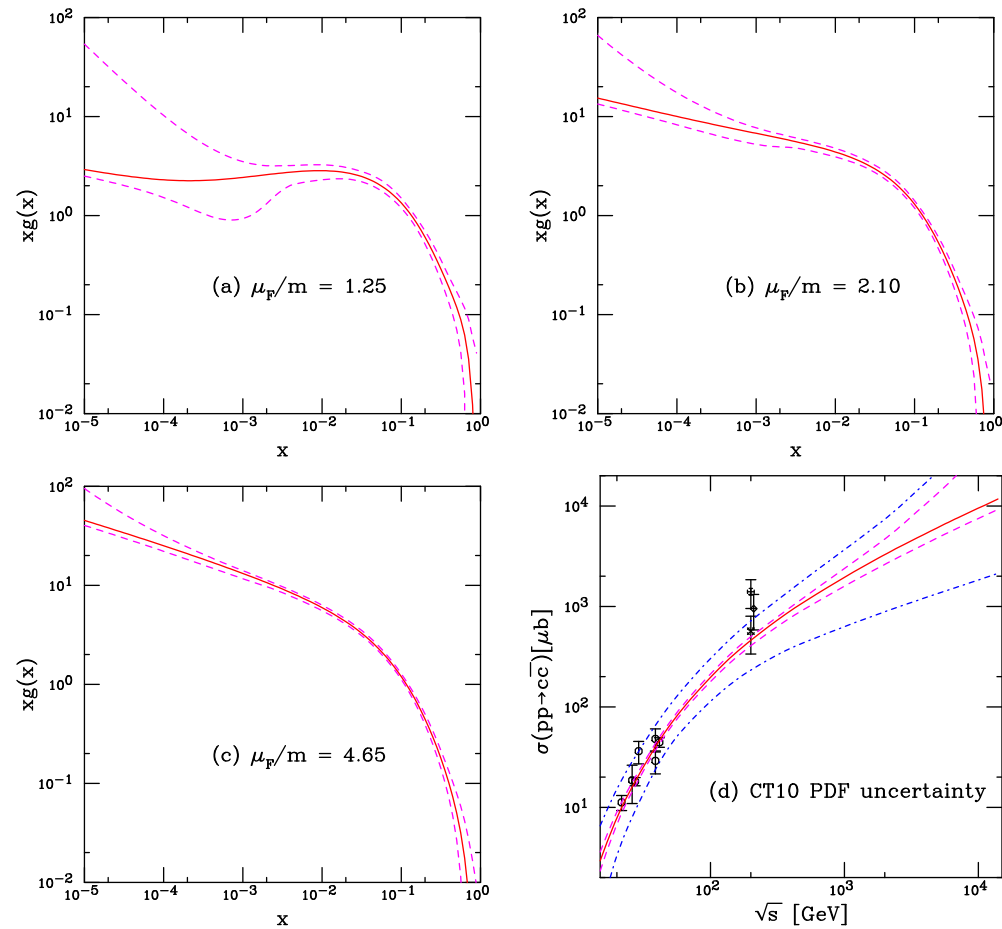


Figure 31: The CT10 gluon distribution,  $xg(x, \mu_F)$ , is shown for the relevant values of  $\mu_F/m$  for the total cross section calculation. The central value of the CT10 gluon distribution is given in the red solid curve while the uncertainty band is denoted by the dashed magenta curves. The results are shown for the lower limit of  $\mu_F/m$ ,  $\mu_F/m = 1.25$  (top left); the central value,  $\mu_F/m = 2.1$  (top right); and the upper limit,  $\mu_F/m = 4.65$  (bottom left). (bottom right) The corresponding uncertainty on the total charm cross section due to the uncertainty in the CT10 gluon distribution is denoted by the dashed magenta lines. The total uncertainty due to the mass and scale uncertainty as well as the gluon uncertainty combined in quadrature is given by the dot-dashed blue curves.

# Results for Heavy Flavor Distributions I: RHIC

Despite narrower uncertainty band for charm (left), relatively good agreement with PHENIX data is obtained (right)

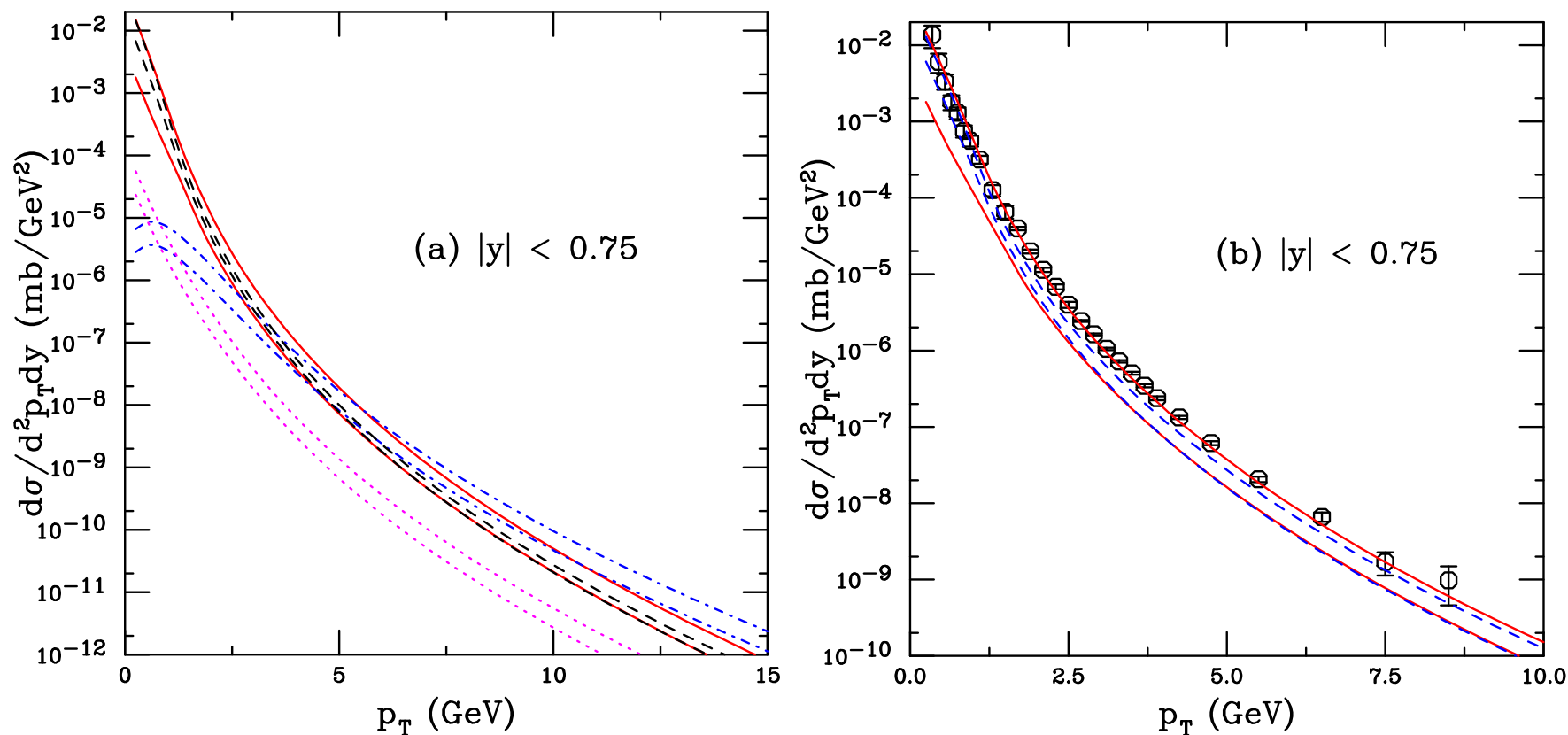


Figure 32: (Color online) (a) The components of the non-photonic electron spectrum:  $B \rightarrow e$  (dot-dashed blue);  $B \rightarrow D \rightarrow e$  (dotted magenta);  $D \rightarrow e$  both with the FONLL parameters (solid red) and those for  $m = 1.27$  GeV (dashed black) at  $|y| < 0.75$  in  $\sqrt{s} = 200$  GeV  $pp$  collisions. (b) The sum of the contributions are compared with the FONLL set for charm (solid red) and  $m = 1.27$  GeV (dashed blue). The PHENIX data are also shown.

# Results on Heavy Flavor Distributions II: LHC

Excellent agreement with  $\sqrt{s} = 7$  TeV ALICE  $pp$  data

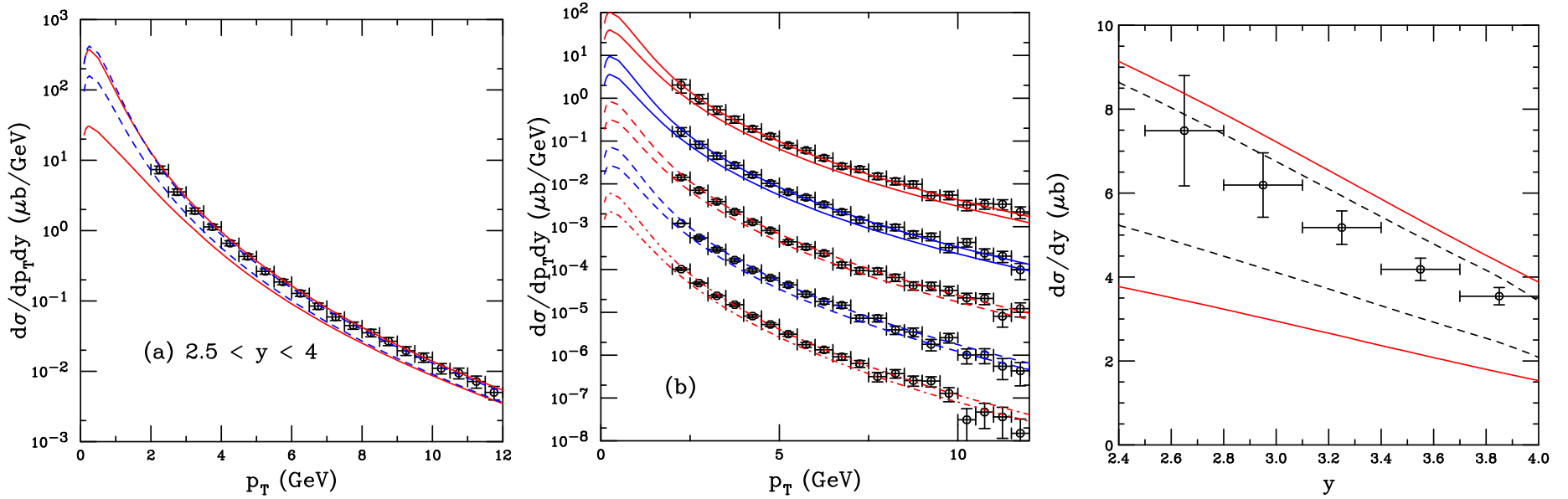


Figure 33: (Left) Comparison of the single lepton  $p_T$  distributions in the rapidity interval  $2.5 < y < 4$  at  $\sqrt{s} = 7$  TeV calculated with the FONLL set for charm (solid red) and the fitted set with  $m = 1.27$  GeV (dashed black). (Center) The contributions to the  $p_T$  distributions in (a) divided into rapidity bins, from top to bottom:  $2.5 < y < 2.8$  (solid red);  $2.8 < y < 3.1$  (solid blue);  $3.1 < y < 3.4$  (dashed red);  $3.4 < y < 3.7$  (dashed blue); and  $3.7 < y < 4$  (dot-dashed red). The top curves are shown at their calculated value, the others are scaled down by successive factors of 10 to separate them. (Right) The sum of the contributions are compared with the FONLL set for charm (solid red) and  $m = 1.27$  GeV (dashed black).

# $J/\psi$ Cross Sections from $c\bar{c}$ Fits

Take results of  $c\bar{c}$  fits, calculate NLO  $J/\psi$  cross section in CEM, fit scale factor  $F_C$   
 Energy dependence almost identical for  $\mu_F = 2m_T$ ,  $\sqrt{s}$  dependence generally better  
 CTEQ6M and CT10 have nearly same value of  $F_C$  so previous results compatible  
 with previous results

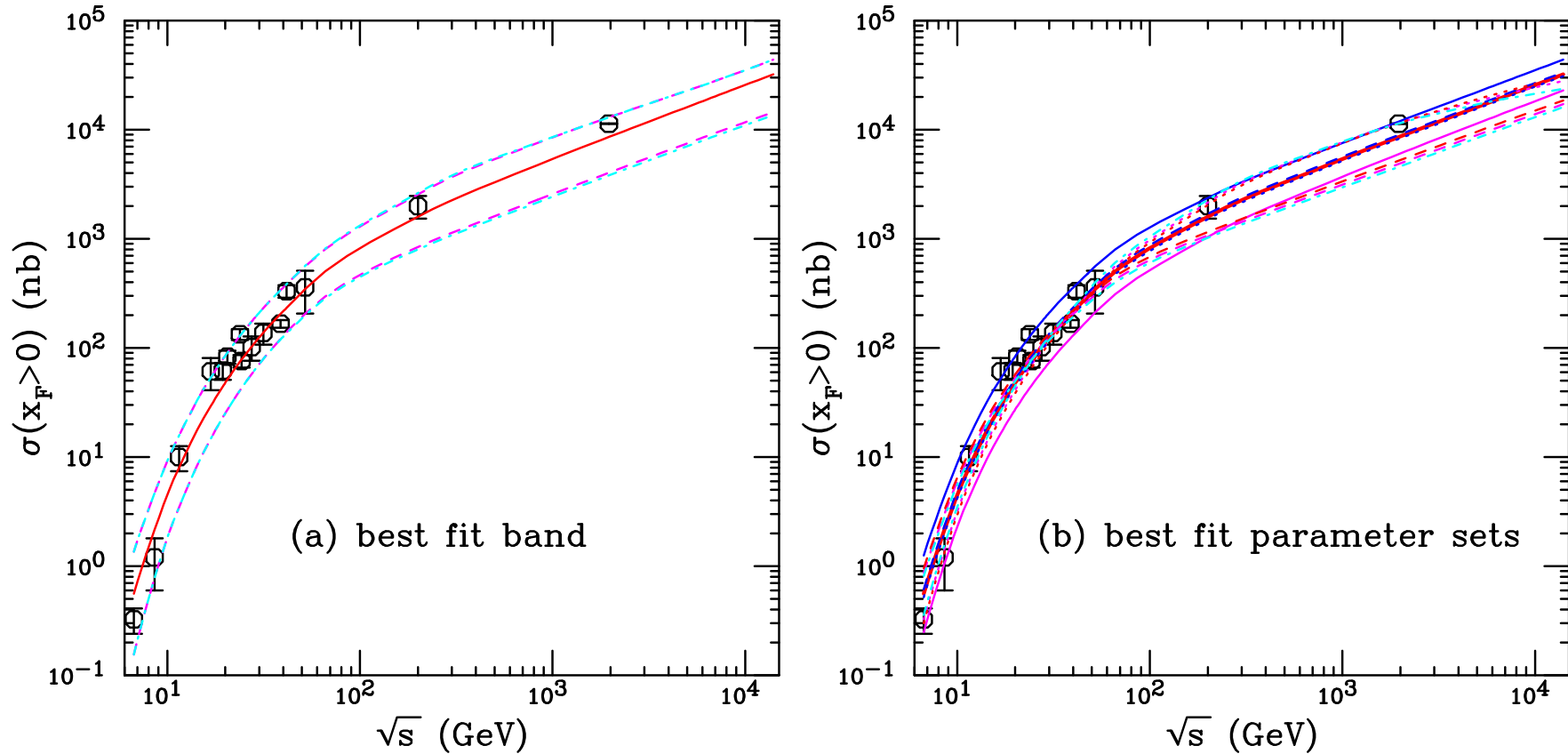


Figure 34: (Left) The uncertainty band on the forward  $J/\psi$  cross section. The dashed magenta curves and dot-dashed cyan curves show the extent of the corresponding uncertainty bands. The dashed curves outline the most extreme limits of the band. (Right) The components of the uncertainty band. The central value ( $m, \mu_F/m_T, \mu_R/m_T$ ) = (1.27 GeV, 2.10, 1.60) is given by the solid red curve. The solid blue and magenta curves outline the mass uncertainty with (1.18 GeV, 2.10, 1.60) and (1.36 GeV, 2.10, 1.60) respectively. The dashed curves outline the lower limits on the scale uncertainty: ( $\mu_F/m_T, \mu_R/m_T$ ) = (2.10, 1.48) blue; (1.25, 1.60) magenta; and (1.25, 1.48) red. The dotted curves outline the upper limits on the scale uncertainty: ( $\mu_F/m_T, \mu_R/m_T$ ) = (2.10, 1.71) blue; (1.25, 1.60) magenta; and (1.25, 1.71) red. The solid black curve is the central value with the scale uncertainty fixed at the central value ( $\mu_F/m_T, \mu_R/m_T$ ) = (2.10, 1.60).

# CEM $p_T$ Distributions

Without intrinsic  $k_T$  smearing (or resummation) the  $Q\bar{Q}$   $p_T$  distribution (LO at  $\mathcal{O}(\alpha_s^3)$  while total cross section is NLO at this order) is too peaked at  $p_T \rightarrow 0$ , needs broadening at low  $p_T$

Implemented by Gaussian  $k_T$  smearing,  $\langle k_T^2 \rangle_p = 1 \text{ GeV}^2$  for fixed target  $pp$  and  $\pi p$ , broadened for  $pA$  and  $AA$ , NLO code adds in final state:

$$g_p(k_T) = \frac{1}{\pi \langle k_T^2 \rangle_p} \exp(-k_T^2 / \langle k_T^2 \rangle_p)$$

Broadening should increase with energy we make a simple linear extrapolation to obtain

$$\langle k_T^2 \rangle_p = 1 + \frac{1}{3n} \ln \left( \frac{\sqrt{s}}{\sqrt{s_0}} \right) \text{ GeV}^2$$

We find  $n \sim 4$  agrees best with RHIC data

Note that unlike FONLL-like calculation of single inclusive heavy flavor with resummed logs of  $p_T/m$ , at large  $p_T$  distribution may be harder than it should be

# CEM Comparison to RHIC $pp$ $J/\psi$ Data

CEM calculation reproduces shape of  $J/\psi$   $p_T$  and  $y$  distributions rather well considering that normalization is set from RHIC energies and below with only one parameter

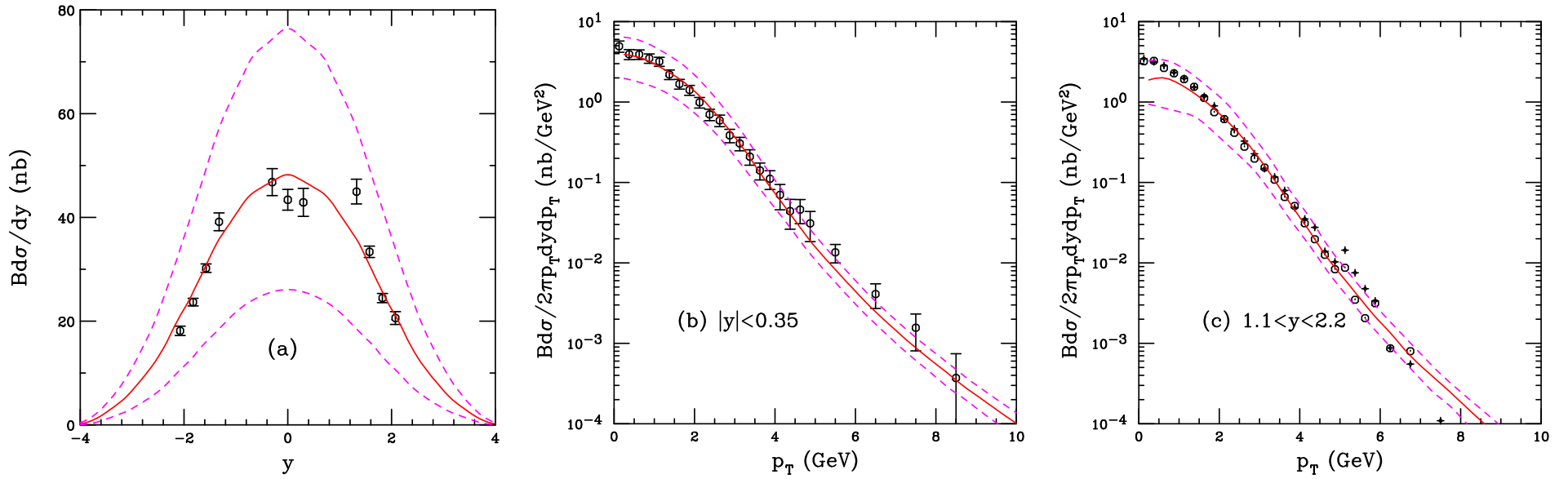


Figure 35: (Color online) The  $J/\psi$  rapidity distribution (a) and the midrapidity (b) and forward rapidity (c)  $p_T$  distributions and their uncertainties. The results are compared to PHENIX  $pp$  measurements at  $\sqrt{s} = 200$  GeV. The solid red curve shows the central value while the dashed magenta curves outline the uncertainty band. A  $\langle k_T^2 \rangle$  kick of 1.19 GeV<sup>2</sup> is applied to the  $p_T$  distributions, as discussed in the text.

# CEM Comparison to LHC 7 TeV $pp$ Quarkonium Data

ALICE 7 TeV  $p_T$  data agree well with calculation for  $p_T > 2$  GeV

Forward rapidity data also within broad uncertainty but seem to want a narrower rapidity distribution overall

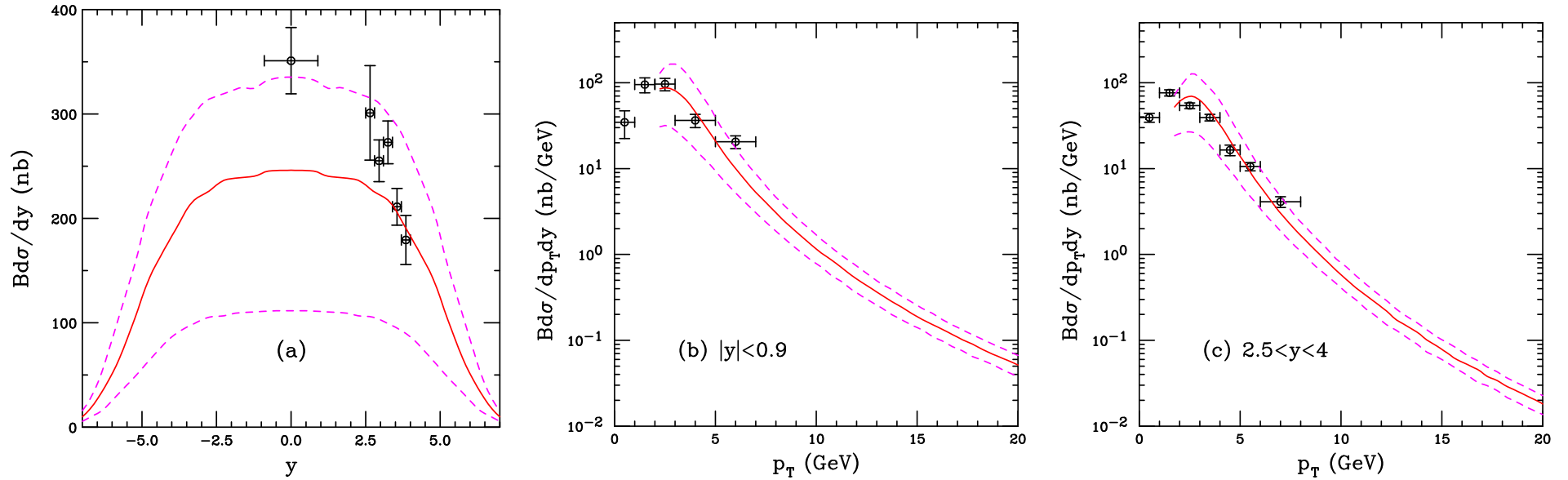


Figure 36: (Color online) The  $J/\psi$  rapidity distribution (a) and the midrapidity,  $|y| < 0.9$  (b), and forward rapidity,  $2.5 < y < 4$  (c)  $p_T$  distributions at  $\sqrt{s} = 7$  TeV and their uncertainties. The results are compared to the ALICE rapidity distribution as well as the mid and forward rapidity  $p_T$  distributions. The solid red curve shows the central value while the dashed magenta curves outline the uncertainty band. A  $\langle k_T^2 \rangle$  kick of  $1.49 \text{ GeV}^2$  is applied to the  $p_T$  distributions, as discussed in the text.

# Comparison to 2.76 TeV LHC $pp$ Quarkonium Data

Overall agreement better at lower energy, including rapidity distribution

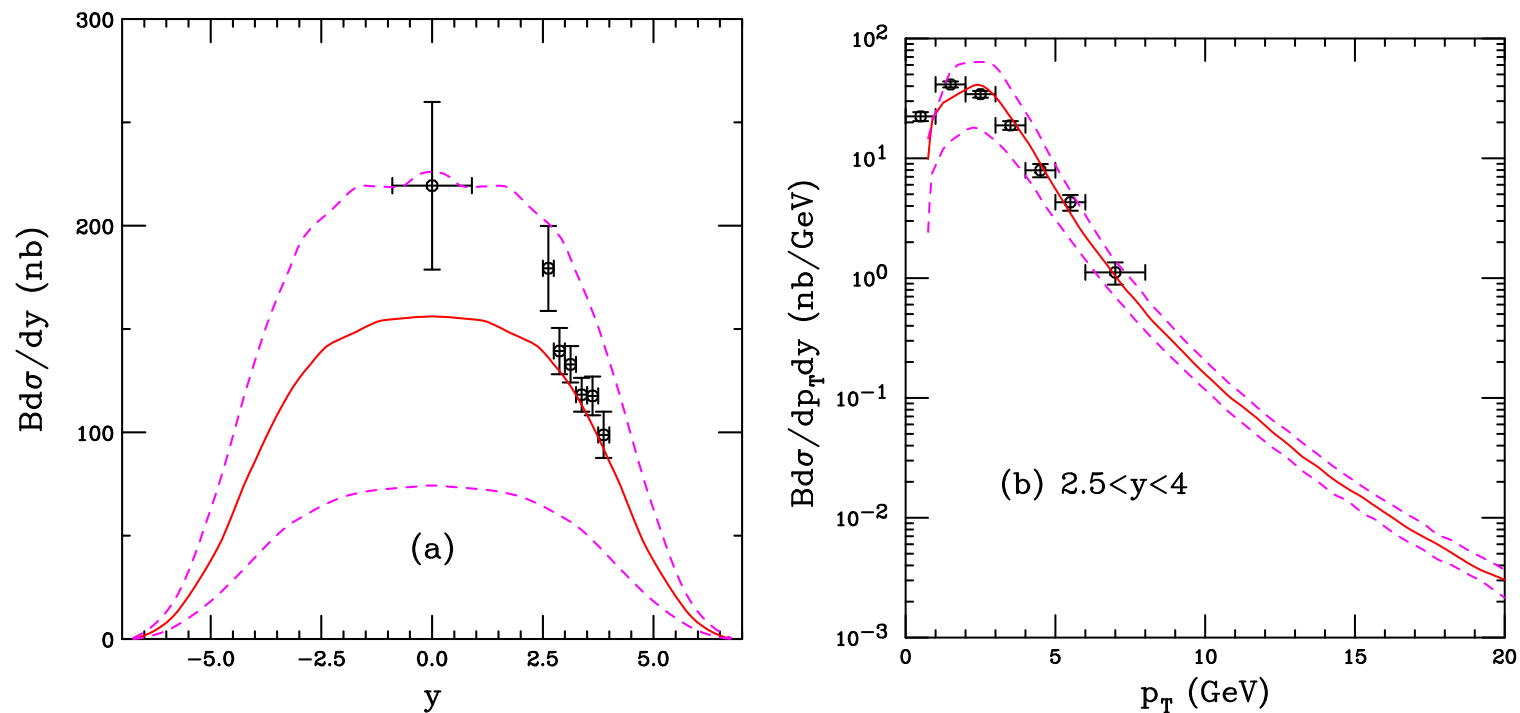


Figure 37: (Color online) The  $J/\psi$  rapidity distribution (a) and the forward rapidity,  $2.5 < y < 4$   $p_T$  distribution (b) at  $\sqrt{s} = 2.76$  TeV and their uncertainties. The results are compared to the ALICE rapidity distribution as well as the forward rapidity  $p_T$  distribution. The solid red curve shows the central value while the dashed magenta curves outline the uncertainty band. A  $\langle k_T^2 \rangle$  kick of  $1.49 \text{ GeV}^2$  is applied to the  $p_T$  distributions, as discussed in the text.

## *pA* and dA Production

# Medium Effects Important with Nuclear Target

Nuclear effects often parameterized as

$$\sigma_{pA} = \sigma_{pp} A^\alpha \quad \alpha(x_F, p_T)$$

For  $\sqrt{s_{NN}} \leq 40$  GeV and  $x_F > 0.25$ ,  $\alpha$  decreases strongly with  $x_F$  – only low  $x_F$  effects probed by SPS and RHIC rapidity coverage

Possible cold matter effects

- Nuclear Shadowing — initial-state effect on the parton distributions affecting total rate, important as a function of  $y/x_F$
- Energy Loss — initial-state effect, elastic scatterings of projectile parton before hard scattering creating quarkonium state, need to study Drell-Yan production to get a handle on the strength when shadowing included
- Intrinsic Charm — initial-state effect, if light-cone models correct, should only contribute to forward production, assumed to have different  $A$  dependence than normal  $J/\psi$  production
- Absorption — final-state effect, after  $c\bar{c}$  that forms the  $J/\psi$  has been produced, pair breaks up in matter due to interactions with nucleons

# Nuclear Modifications of the Parton Densities

# Parton Densities Modified in Nuclei

Nuclear deep-inelastic scattering measures quark modifications directly, gluon modifications only through  $Q^2$  dependence of  $F_2$

More uncertainty in nuclear gluon distribution

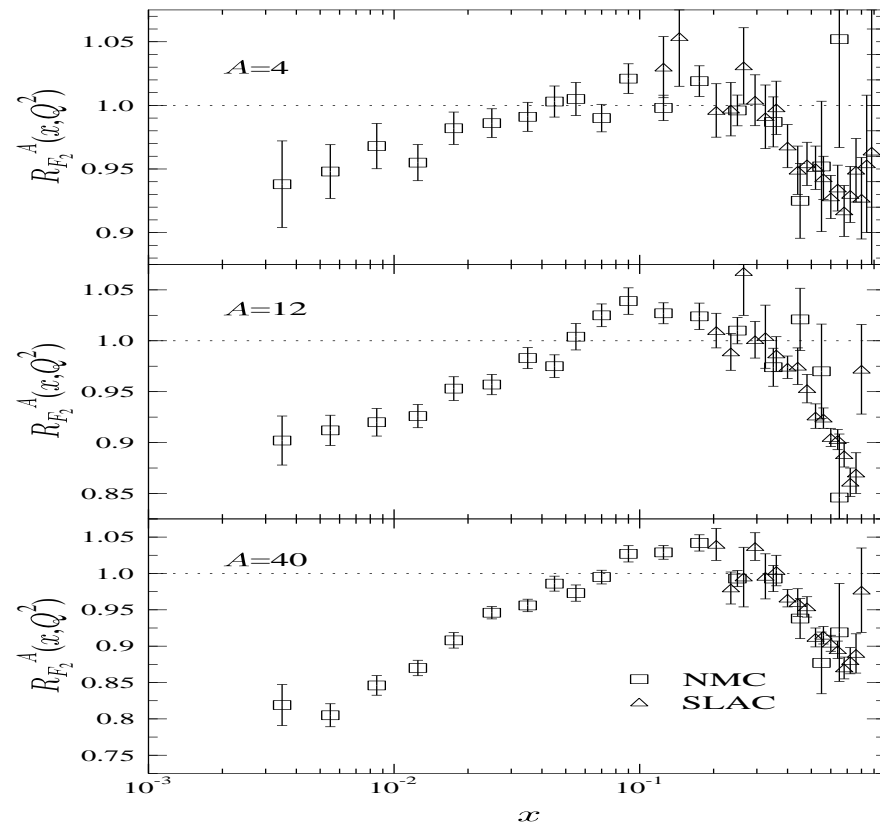


Figure 38: Ratios of charged parton densities in He, C, and Ca to D as a function of  $x$ . [From K.J. Eskola.]

# Shadowing Parameterizations On The Market

- EKS98:** K. J. Eskola, V. J. Kolhinen and P. V. Ruuskanen, Nucl. Phys. B 535 (1998) 351 [arXiv:hep-ph/9802350]; K. J. Eskola, V. J. Kolhinen and C. A. Salgado, Eur. Phys. J. C 9 (1999) 61 [arXiv:hep-ph/9807297].
- nDS:** D. de Florian and R. Sassot, Phys. Rev. D 69, 074028 (2004) [arXiv:hep-ph/0311227].
- HKN:** M. Hirai, S. Kumano and T. H. Nagai, Phys. Rev. C 70, 044905 (2004) [arXiv:hep-ph/0404093].
- FGS:** L. Frankfurt, V. Guzey and M. Strikman, Phys. Rev. D 71 (2005) 054001 [arXiv:hep-ph/0303022].
- EPS08:** K. J. Eskola, H. Paukkunen and C. A. Salgado, JHEP 0807, 102 (2008) [arXiv:0802.0139 [hep-ph]].
- EPS09:** K. J. Eskola, H. Paukkunen and C. A. Salgado, JHEP 0904 (2009) 065 [arXiv:0902.4154 [hep-ph]].

## Differences Between Eskola *et al* Sets

**EKS98** Simple parameterization for all  $A$ ; leading order analysis only; GRV LO set used for proton PDFs; single set; **no  $\chi^2$  analysis performed**;  $2.25 \leq Q^2 \leq 10^4 \text{ GeV}^2$ ;  $10^{-6} < x < 1$

**EPS08** Simple parameterization for all  $A$ ; leading order analysis only; CTEQ61L set used for proton PDFs; single set;  **$\chi^2$  analysis uses forward BRAHMS data from RHIC to maximize gluon shadowing**;  $1.69 \leq Q^2 \leq 10^6 \text{ GeV}^2$ ;  $10^{-6} < x < 1$

**EPS09** Available for select  $A$  values; LO and NLO sets available based on CTEQ61L and CTEQ6M respectively;  **$\chi^2$  analysis done at both LO and NLO**; calling routine similar to other sets but now there are 31, 15 above and 15 below the central set; **no longer use BRAHMS data**

If  $\chi^2$ -minimized set of parameters,  $\{a_0\}$ , gives best estimate of nPDFs, work in a basis  $\{z\}$  that diagonalizes covariance matrix, errors in nPDFs computed within 90% confidence criteria,  $\Delta\chi^2 = 50$

Upper and lower uncertainties in any observable  $X$  can be computed using the prescription

$$\begin{aligned}(\Delta X^+)^2 &\approx \sum_k \left[ \max \{ X(S_k^+) - X(S^0), X(S_k^-) - X(S^0), 0 \} \right]^2 \\ (\Delta X^-)^2 &\approx \sum_k \left[ \max \{ X(S^0) - X(S_k^+), X(S^0) - X(S_k^-), 0 \} \right]^2\end{aligned}$$

In all cases, when  $A$ ,  $x$  or  $Q^2$  are outside the range of validity, the last value is returned, *e.g.* if  $x < 10^{-6}$  value at  $x = 10^{-6}$  is given

# $Q^2$ Dependence of EPS09 – Constrains Gluon

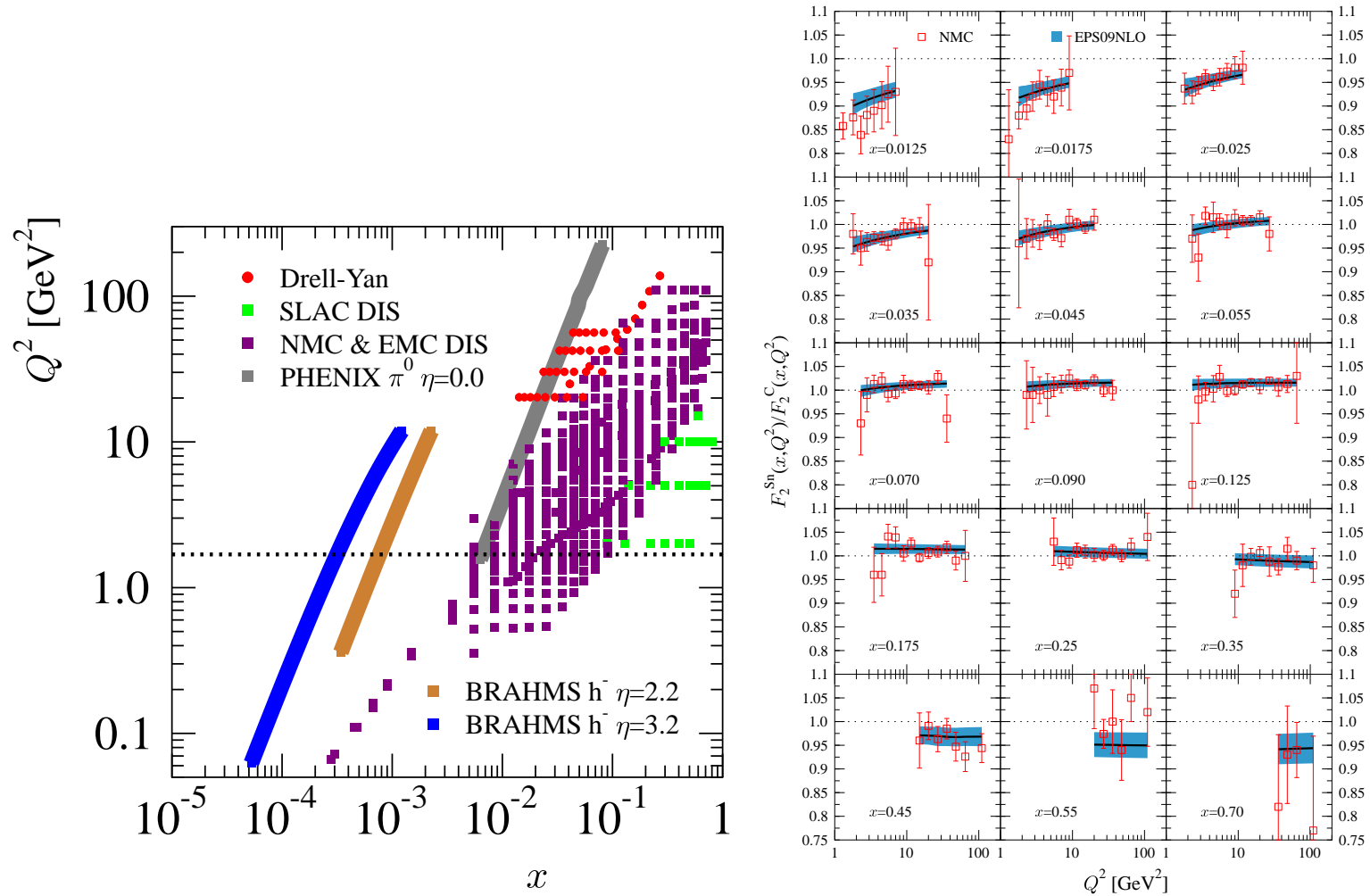


Figure 39: Left: initial gluon distributions at  $Q_0^2 = 1.4 \text{ GeV}^2$ . Right: evolution of gluon distributions for several fixed values of  $x$  shows that the effect of the nonlinear terms vanishes as  $Q^2$  increases.

## $x$ Dependence of EPS09

Note that the width of the uncertainty band can be bigger than any individual ratio since the errors added in quadrature

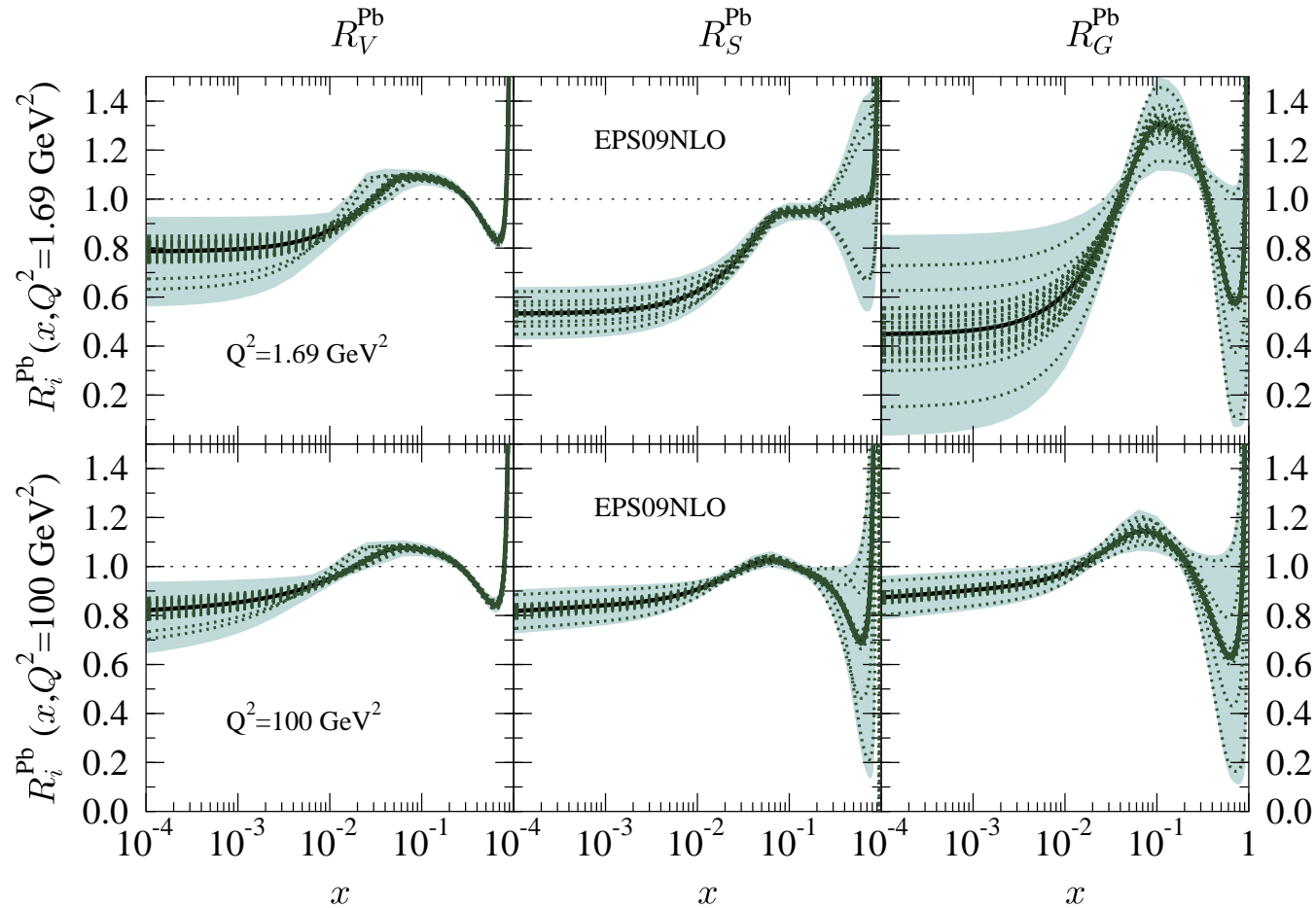


Figure 40: Left: initial gluon distributions at  $Q_0^2 = 1.4 \text{ GeV}^2$ . Right: evolution of gluon distributions for several fixed values of  $x$  shows that the effect of the nonlinear terms vanishes as  $Q^2$  increases.

# Comparison of LO and NLO nDS nPDFs

While the magnitude of the absolute cross sections may differ at LO and NLO, the effect of shadowing is, by design, the same at LO and NLO as long as data are included in the fit

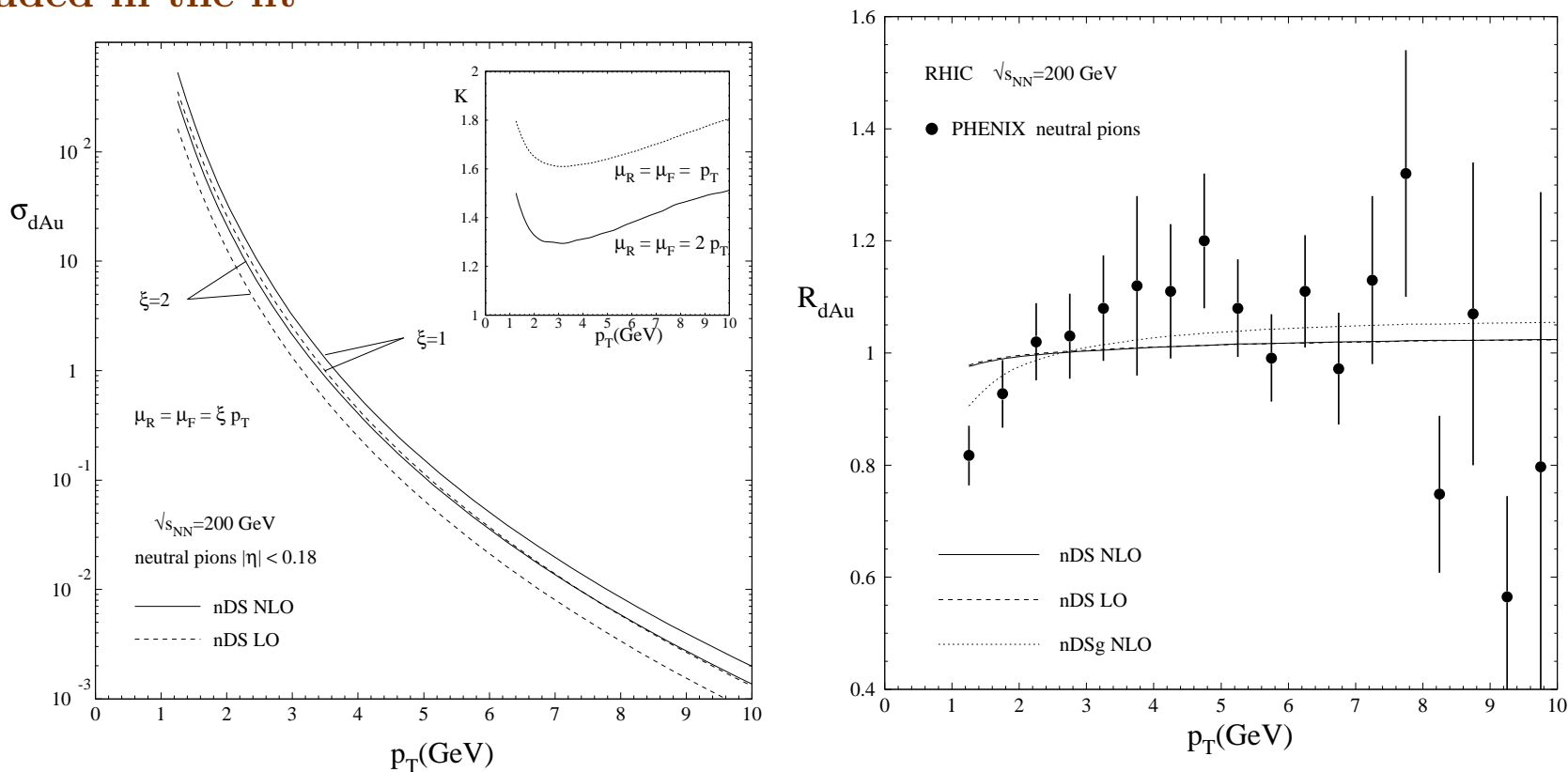


Figure 41: Left: The  $\pi^0$  cross section in d+Au collisions at  $\sqrt{s_{NN}} = 200$  GeV at LO and NLO. Right: The LO and NLO calculations of  $R_{dAu}$ .

# Comparing Shadowing Parameterizations: $x$ Dependence

EKS98, EPS08 and nDSg available for all  $A$ , HKN for select nuclei

EKS98 and EPS08 have strong antishadowing at  $x \sim 0.1$ , nDSg has almost none

EPS08 stronger at low  $x$  than others to fit forward BRAHMS data  $A$

EPS09 provides uncertainty band at LO and NLO; central value of gluon shadowing like EKS98, lower limit like EPS08, upper limit like nDSg

Increasing  $\sqrt{s}$  broadens rapidity range, decreases  $x_2$

Midrapidity fixed-target energies in antishadowing range; RHIC coverage spans shadowing to antishadowing regions

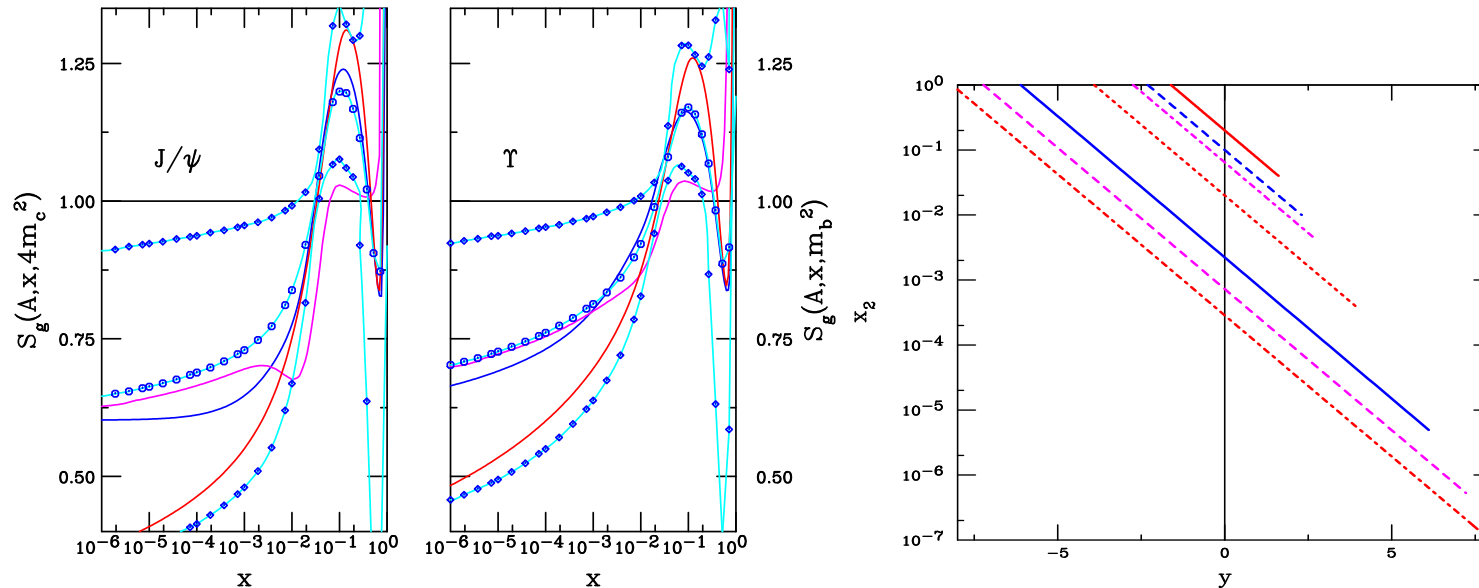


Figure 42: (Left) EKS98 (blue), nDSg (magenta), EPS08 (red) and EPS09 (cyan, blue dots) gluon shadowing parameterizations for  $J/\psi$  (left-hand side) and  $\Upsilon$  (right-hand side) production scales for  $A = \text{Pb}$ . (Right) The average value of  $x_2$  in  $pp$  collisions as a function of rapidity for (top to bottom)  $\sqrt{S_{NN}} = 20; 40; 62; 200; 1800; 5500$  and  $14000$  GeV.

# Comparison of LO and NLO EPS09 Gluon nPDFs

Nuclear gluon density not as well constrained at finite scales as are quark distributions

LO EPS09 shadowing ratio has a wider antishadowing region and bigger uncertainty in EMC region ( $x > 0.3$ )

At low  $x$ ,  $x < 0.01$ , the uncertainty in shadowing is smaller at NLO

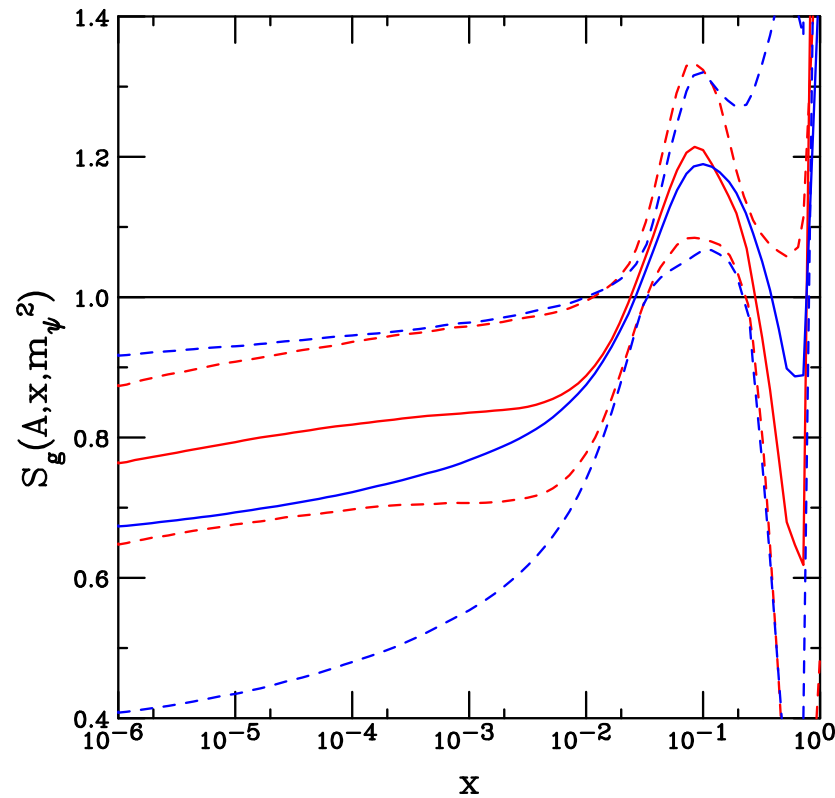


Figure 43: The modification of the gluon densities at LO (blue) and NLO (red) with EPS09, including uncertainties (dashed lines), calculated at  $m_\psi$ .

# Effects on the $J/\psi$ Cross Section

Both ratios calculated in the CEM

Left side: calculated with LO EKS98 parameterization with both LO ( $2 \rightarrow 1$ ) and NLO ( $2 \rightarrow 2$ ) kinematics – ratios are the same within statistics

Right side: LO ratio (blue) calculated with EPS09 LO shadowing; NLO ratio is calculated with EPS09 NLO shadowing

Newer calculation shows a difference because the LO and NLO gluon shadowing is different with EPS09 and not well enough constrained to make the ratios more similar, as opposed to quark-dominated observables

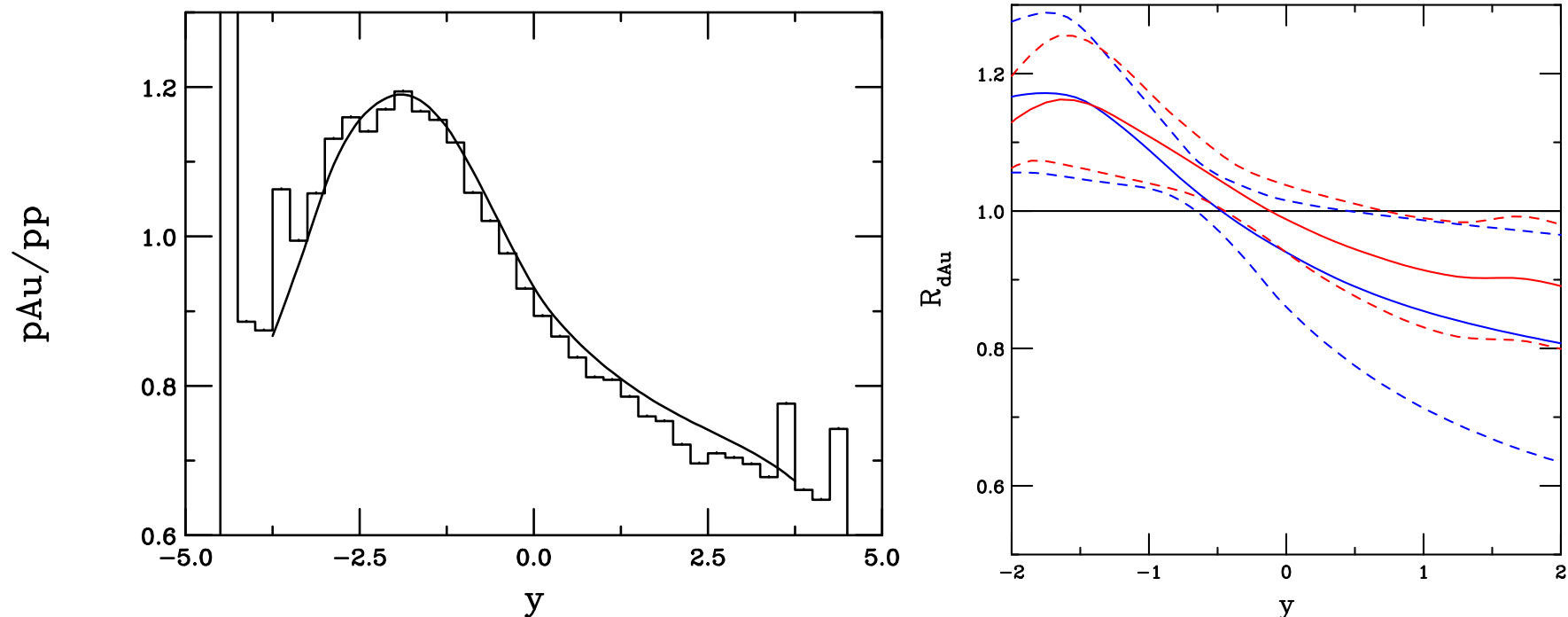


Figure 44: Left: The ratio  $R_{dAu}$  at  $\sqrt{s_{NN}} = 200$  GeV at LO and NLO with the EKS98 parameterization. Right: The LO and NLO calculations of  $R_{dAu}$ .

# NLO Scale Dependence Smaller than nPDF Dependence

Left side: Red band shows variation with EPS09 NLO shadowing; blue band takes central EPS09 set and presents mass and scale variations for that set

Center: variation in EPS09 LO shadowing due to varying charm quark mass  $1.18 < m < 1.36$  GeV

Right: variation in EPS09 LO shadowing with  $\mu_F/m = 1.25, 2.10$  and  $4.65$ , limits of factorization

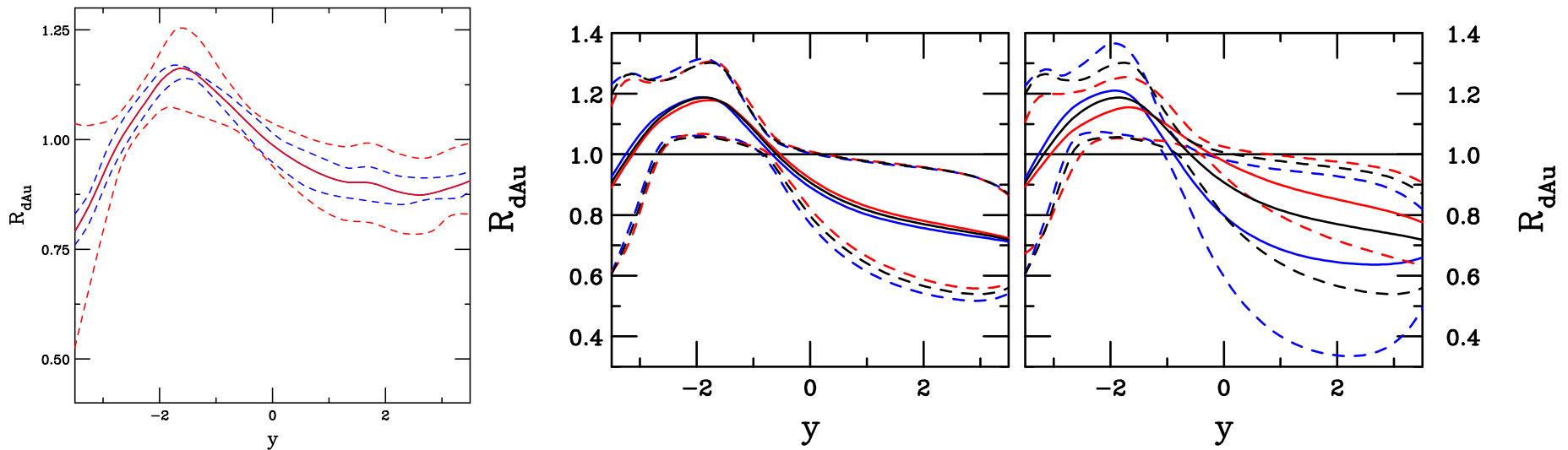


Figure 45: Left: The scale variation of  $R_{dAu}$  with the central EPS09 set (blue) compared to the EPS09 variation for the central parameter set (red). Right: The EPS09 uncertainty band in 200 GeV d+Au collisions at RHIC for (left)  $m = 1.18$  (blue), 1.27 (black), and 1.36 (red) GeV with the central scale values and for (right)  $m = 1.27$  GeV with  $\mu_F/m = 2.8$  (black), 1.41 (blue) and 5.91 (red).

# Extrinsic vs. Intrinsic $J/\psi$ Production

Both ratios calculated in the CEM

LO CEM calculation on left equivalent to 'intrinsic' calculation with  $p_T = 0$  on right-hand side

Including average  $p_T$  in scale of LO CEM shifts shape somewhat, amount of shift depends on assumed scale

'Extrinsic' calculation is LO CSM, results similar to central value of NLO CEM result on left-hand side

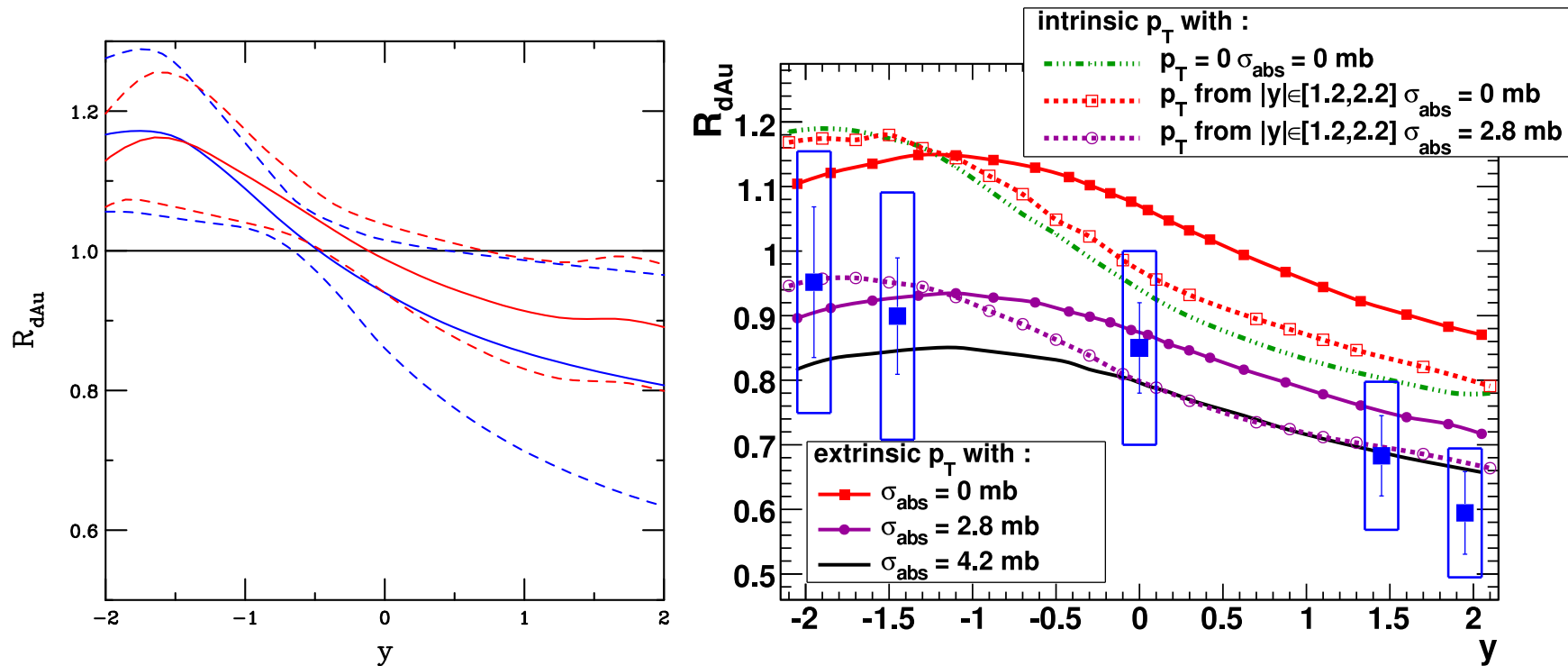


Figure 46: Left: The  $\pi^0$  cross section in d+Au collisions at  $\sqrt{s_{NN}} = 200$  GeV at LO and NLO. Right: The LO and NLO calculations of  $R_{dAu}$ .

# $p_T$ Dependence of Shadowing Accessible at NLO

Both d+Au and  $pp$   $p_T$  dependence calculated with same intrinsic  $k_T$  kick

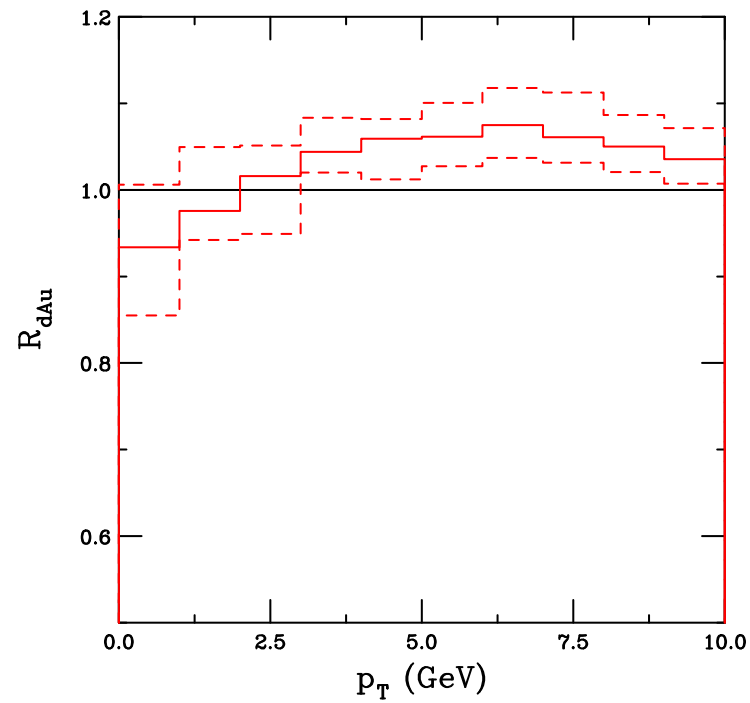


Figure 47: The ratio  $R_{dAu}$  at  $\sqrt{s} = 200$  GeV.

# Final-State Absorption

# Quarkonium Absorption by Nucleons

Woods-Saxon nuclear density profiles typically used

$$\begin{aligned}\sigma_{pA} &= \sigma_{pN} \int d^2b \int_{-\infty}^{\infty} dz \rho_A(b, z) S_A^{\text{abs}}(b) \\ &= \sigma_{pN} \int d^2b \int_{-\infty}^{\infty} dz \rho_A(b, z) \exp \left\{ - \int_z^{\infty} dz' \rho_A(b, z') \sigma_{\text{abs}}(z' - z) \right\}\end{aligned}$$

Note that if  $\rho_A = \rho_0$ ,  $\alpha = 1 - 9\sigma_{\text{abs}}/(16\pi r_0^2)$

The value of  $\sigma_{\text{abs}}$  depends on the parameterization of  $\sigma_{pA}$  – Glauber, hard sphere,  $A^\alpha$  etc. (shown by NA50)

Initial-state shadowing only recently taken into account at SPS energies

Feed down to  $J/\psi$  from  $\chi_c$  and  $\psi'$  decays not always included, should dictate that

$$\sigma_{pA} = \sigma_{pN} \int d^2b [0.6S_{\psi, \text{dir}}(b) + 0.3S_{\chi_c J}(b) + 0.1S_{\psi'}(b)]$$

Each charmonium state should interact with a different asymptotic absorption cross section, not yet included; formation time dependence yet to be incorporated

The  $\chi_c$   $A$  dependence remains unknown

# Production Model Dependence of Nuclear Absorption

Color singlet absorption assumes that each charmonium state interacts with a different constant asymptotic absorption cross section,

$$\sigma_{\text{abs}}^C = \sigma_{\text{abs}}^{J/\psi} \left( \frac{r_C}{r_{J/\psi}} \right)^2$$

Measurements from SPS to RHIC suggest that absorption decreases with increasing energy while shadowing effects increase

Predictions that quarkonium absorption cross sections decrease with energy agree with trend of data [Braun *et al.*, Nucl. Phys. B 509 (1998) 357 (hep-ph/9707424), Capella and Ferreiro (hep-ph/0610313)]

Octet cross section assumed to be constant as a function of rapidity

NRQCD contains elements with octet and singlet absorption, predicts different  $A$  dependence for  $\chi_c$  and  $J/\psi$ ,  $\psi'$  depending on relative mix of octet and singlet production

Absorption alone always gives less than linear  $A$  dependence ( $\alpha < 1$ )

# A Dependence of $J/\psi$ and $\psi'$ Not Identical

Color octet mechanism suggested that  $J/\psi$  and  $\psi'$   $A$  dependence should be identical — Supported by large uncertainties of early data

More extensive data sets (NA50 at SPS, E866 at FNAL) show clear difference at midrapidity [NA50  $\rho L$  fit gives  $\Delta\sigma = \sigma_{\text{abs}}^{\psi'} - \sigma_{\text{abs}}^{J/\psi} = 4.2 \pm 1.0$  mb at 400 GeV,  $2.8 \pm 0.5$  mb at 450 GeV for absolute cross sections]

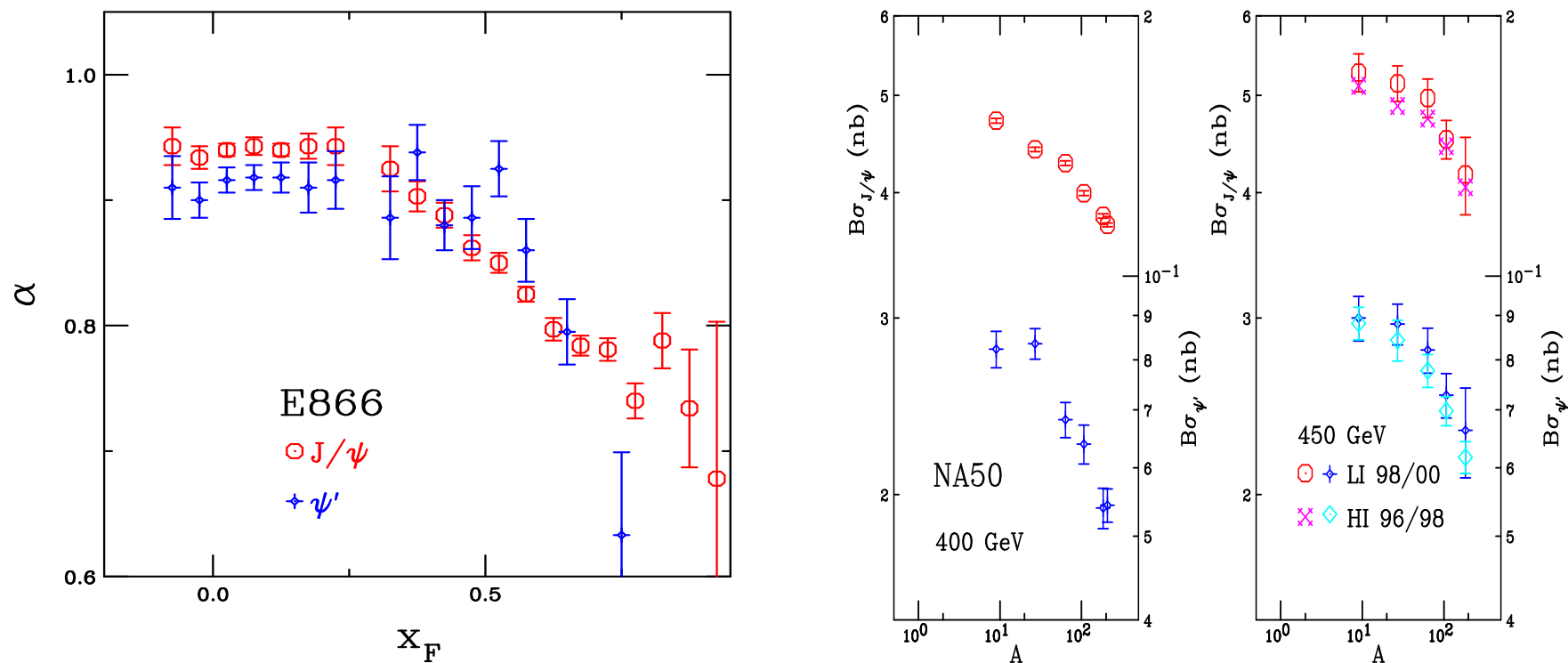


Figure 48: The  $J/\psi$   $A$  dependence (left) as a function of  $x_F$  at FNAL ( $\sqrt{s_{NN}} = 38.8$  GeV) and (right) and a function of  $A$  at the SPS (NA50 at  $p_{\text{lab}} = 400$  and 450 GeV) for  $J/\psi$  and  $\psi'$  production.

# Interplay of Shadowing and Absorption

Depending on  $x$  values probed, including shadowing can enhance or reduce absorption cross section,  $\sigma_{\text{abs}}$ , needed to describe data

For SPS energies,  $17.3 \leq \sqrt{S} \leq 29$  GeV, antishadowing region,  $pA/pp > 1$  with no absorption: including shadowing requires larger  $\sigma_{\text{abs}}$  to agree with data

For  $\sqrt{S} \geq 38$  GeV, shadowing regime,  $pA/pp < 1$  with shadowing alone at  $y > 0$ , smaller  $\sigma_{\text{abs}}$  needed

Assume initial-state shadowing and absorption survival probability factorize

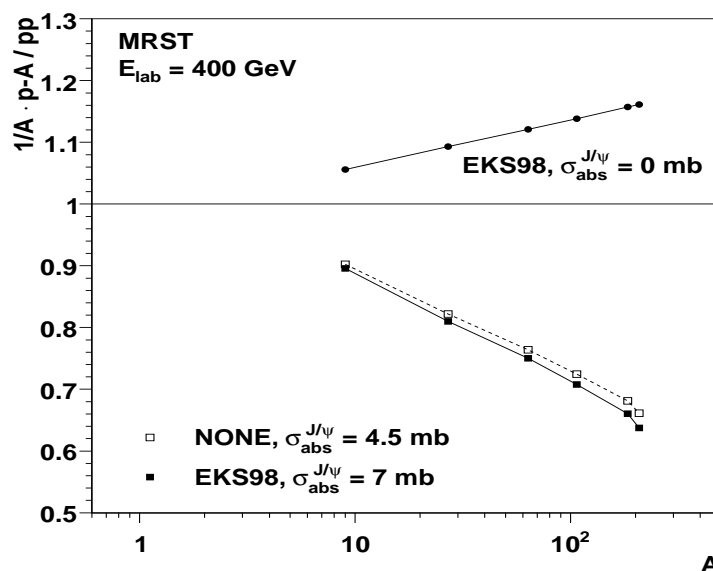


Figure 49: Illustration of the interplay between shadowing and absorption. [C. Lourenco, H. K. Wohri and RV, JHEP **0902** (2009) 014.]

# Apparent Energy Dependence of $\sigma_{\text{abs}}$ , Independent of Shadowing Parameterization

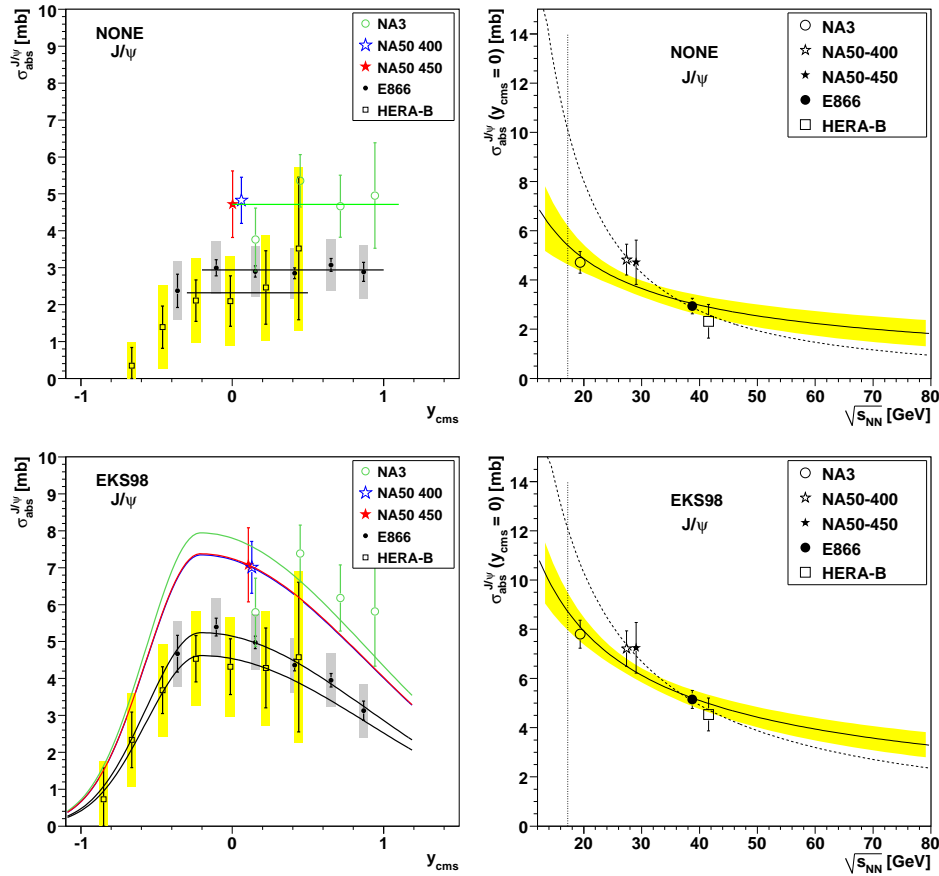


Figure 50: (Left)  $\sigma_{\text{abs}}^{J/\psi}$  as a function of  $y_{\text{cms}}$ , obtained without and with shadowing. The boxes represent the total errors. When nuclear PDFs are used, the E866 and HERA-B absorption patterns depend on  $y_{\text{cms}}$ . (Right) Dependence of  $\sigma_{\text{abs}}^{J/\psi}(y_{\text{cms}}=0)$  on  $\sqrt{s_{NN}}$ . The curves represent power-law fits, with (solid line with error band) and without (dashed line) the NA3 point. [C. Lourenco, H. K. Wohri and RV, JHEP **0902** (2009) 014.] Predicts  $5 \leq \sigma_{\text{abs}} \leq 8$  mb for 158 GeV  $pA$ .

# NA60 $pA$ Data Consistent With Predictions

Previously assumed that  $\sigma_{\text{abs}} = 4.2 \pm 0.5$  mb at 158 GeV ( $AA$  energy), obtained from 400 and 450 GeV data, independent of  $\sqrt{S_{NN}}$

New NA60  $pA$  data at 158 GeV find significantly higher  $\sigma_{\text{abs}}$ :  $7.6 \pm 0.7 \pm 0.6$  mb without shadowing and  $9.3 \pm 0.7 \pm 0.7$  with EKS98

Larger baseline absorption cross section means less ‘anomalous’ suppression in  $AA$

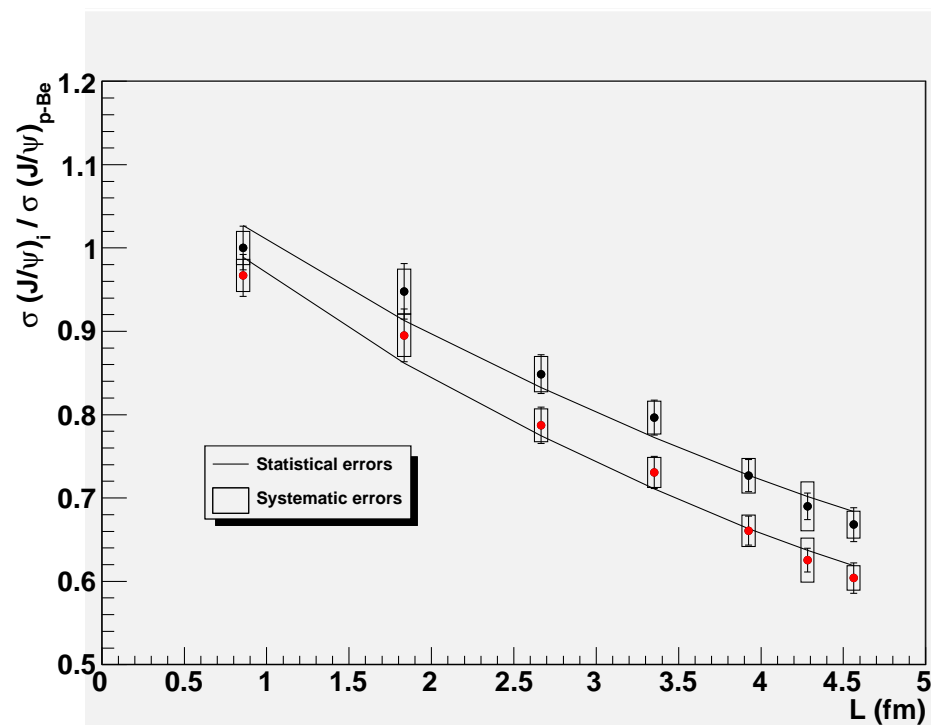


Figure 51: Preliminary NA60 data on  $J/\psi$  absorption at 158 GeV. The red points show the results for free proton PDFs (no nuclear effects) while the black points have the relevant antishadowing effect removed before fitting  $\sigma_{\text{abs}}$ . (The path length  $L$  is the distance the  $J/\psi$  travels through matter,  $L \propto (3/4)R_A$ .) [Thanks to E. Scomparin, NA60.]

## Summary

- Understanding of production mechanism has evolved but still not settled
- Fitting the scale parameters to the total charm cross section data significantly reduces the uncertainties on both open charm and  $J/\psi$
- Production mechanism affects interpretation of  $pA$ ,  $dA$  data
- Significant differences between LO and NLO shadowing with EPS09 parameterization
- Data seem to suggest absorption cross section decreases with  $\sqrt{s_{NN}}$